Thermal Large Eddy Simulation in a Very Simplified Geometry of a Solar Receiver

Sylvain Serra, Adrien Toutant, Françoise Bataille

To cite this version:

Sylvain Serra, Adrien Toutant, Françoise Bataille. Thermal Large Eddy Simulation in a Very Simplified Geometry of a Solar Receiver. Heat Transfer Engineering, 2012, 33 (6), pp.505-524. 10.1080/01457632.2012.624856 . hal-02102334

HAL Id: hal-02102334
https://hal.science/hal-02102334v1

Submitted on 13 Sep 2024

Thermal Large Eddy Simulation in a Very Simplified Geometry of a Solar Receiver

SYLVAIN SERRA, ADRIEN TOUTANT, and FRANÇOISE BATAILLE
Laboratoire PROMES, Rambla de la thermodynamique, Tecnosud, Perpignan, France

Thermal large eddy simulations are carried out in order to study the convective flow in a solar receiver. We investigate the impact of thermal gradients on a turbulent channel flow with imposed wall temperatures for two turbulent Reynolds numbers based on the friction velocity (180 and 395). In this configuration, the flow is subsonic, while temperature variations can be strong and induce significant variations of the fluid properties. The low Mach number equations are considered. The influence of the variations of the conductivity and the viscosity is first investigated. We show that the influence of these properties can be considered constant only for weak temperature gradients. The thermal subgrid-scale modeling is studied and we conclude that for a temperature ratio of 2, we can use a constant subgrid-scale Prandtl number. Finally, we focus on the increase of the temperature ratio that emphasizes the flow dissymmetry and modifies the fluctuations profiles. The physical mechanism responsible for these modifications is explained.

INTRODUCTION

In many industrial configurations there is a coupling between heat transfer and fluid mechanics (nuclear power plants, heat exchangers, solar power plants, etc.). The concerned industrial application of the fundamental study of this article is high-temperature solar receivers. The receiver is a key component of solar power tower plant. The working principle of this plant is the following (Figure 1). The solar energy is concentrated on the receiver (located on top of the tower) by a field of heliostats (i.e., mirrors that track the movement of the sun). Then this thermal energy is held by a turbulent airflow that transits across the receiver. Finally, the heated airflow enters a gas turbine to create electricity.

The efficiency of the solar power plant is directly linked to thermodynamic cycle: It increases with temperature. This implies very strong heat transfer and consequently relatively high velocity and turbulence intensity in the solar receiver. The solar receiver is based on the compact heat exchanger technologies. It will be composed by many channels for which only one wall is heated. Typically, in these channels, the heating is asymmetric, the Mach number is approximately equal to 0.1, the bulk Reynolds number goes from 4000 to 40,000, and the Richardson number goes to 0.0001. Therefore, the physical conditions of interest correspond to low Mach number and forced convective heat transfer. The fundamental study presented in this article concerns a turbulent channel flow with imposed temperature at the wall. A cold temperature $T_1 = 293$ K is imposed at the non-heated wall. A hot temperature T_2 (with $T_2 > T_1$) is imposed at the heated wall. The realized parametric study considers bulk Reynolds numbers (Eq. (23)) that go from 2800 to 7500 and temperature ratios (T_2/T_1) from 1 to 2 (Table 1). The chosen ranges for both bulk Reynolds numbers and temperature ratios are relevant for the concerned application.

Although there is no direct numerical simulation or large eddy simulation dedicated to solar power plants in the literature, a lot of work concerns non-isothermal turbulent flows. Several numerical studies taking density, conductivity, and viscosity variations into account are compressible simulations of supersonic flows (conjugate effects of anisothermy and compressibility). Huang et al. [1], for example, have carried out some direct numerical simulations (DNS) of a channel flow with very cold isothermal walls at a low turbulent Reynolds number for two Mach numbers (1.5 and 3). They studied the averaging, the semilocal scaling, and energy transfers, but they

We acknowledge the support of the CINES (France), which provided us computer resources to carry out our simulations. We are also thankful to the CEA (France Atomic Agency), for its support with Trio U code.

Address correspondence to Professor Françoise Bataille, PROcédés, Matériaux et Energie Solaire (UPR CNRS 8521), Rambla de la thermodynamique, Tecnosud, 66100 Perpignan, France. E-mail: francoise.bataille@promes.cnrs.fr

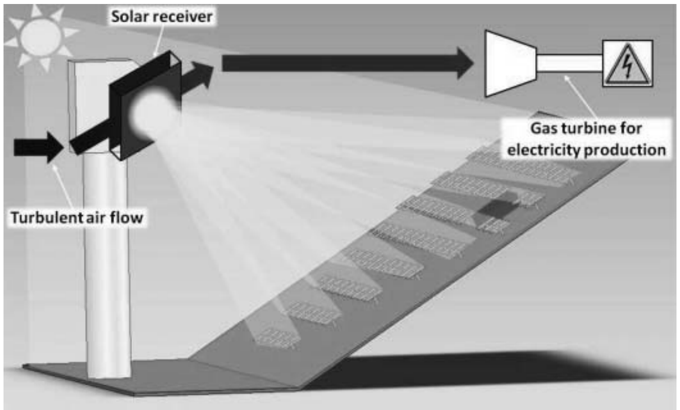

Figure 1 Working principle of the solar power plant.

did not investigate the impact of the temperature gradient on the flow. Coleman et al. [2] have also studied this configuration by DNS. They mainly focused on the Mach number influence and showed that Morkovin's hypothesis holds for this kind of flow. Like Huang et al. [1], they found that a semilocal scaling permits a good collapse of the different profiles onto the incompressible data. Similar compressible DNS have been carried out by Morinishi et al. [3] and Tamano and Morinishi [4] in order to determine the effect of the thermal boundary conditions on a turbulent channel flow (isothermal or adiabatic walls). The simulations carried out by Wang and Pletcher [5] concern a turbulent channel flow with imposed temperature at the wall. Temperature ratios (T_2/T_1) of 1.02 and 3 have been considered. The increase of T_2/T_1 is shown to influence the fluctuation velocity and temperature distribution as well as the velocity–temperature correlations. The correlation of the velocity and temperature fluctuations appears stronger near the heated wall and weaker near the cold wall.

We here focus on low-speed flows (Mach number lower than 0.1) submitted to thermal gradients that induce large variations of the fluid properties. We therefore consider a particular set of equations, the low Mach number equations. These equations are the most appropriate to study such flows because they permit to remove the acoustic waves, and thus relieve us of the acoustic constraints on the time steps, but do not limit the temperature difference of the configuration as Boussinesq's assumption does. Numerical studies with a low Mach number and a significant thermal gradient can be found in the literature [6–13]. However, in most of these works, the temperature effect is not isolated. For example, some DNS and thermal large eddy simulations have been carried out to study low-speed flows with strong property variations in vertical pipes with heated walls [14–18]. In this case, the effects of fluid property variations with the temperature are combined with the buoyancy influence. The subsonic channel flow with significant heat transfer has been investigated by Dailey et al. [6] using compressible simulations. Due to the constant heat flux imposed at the walls, the temperature increases continuously during their simulations and an appropriate recycling condition has been established for the temperature in this case. The use of semilocal coordinates is shown to better collapse the mean profiles onto the incompressible log laws. This study is very different from ours because there is no transverse thermal gradient (the two walls have the same temperature). In their study, the turbulent shear stress and heat flux seem to be reduced by heating and increased by cooling.

In the present article, we investigate turbulent forced convection using thermal large eddy simulation applied to low Mach number equations [7–9]. The DNS based on the low Mach number equations, carried out by Nicoud [19, 20] and Debusschere and Rutland [10], and the low Mach number large eddy simulation (LES) of Lessani and Papalexandris [11, 12] deal with the same configuration. Lessani and Papalexandris [12] have simulated a channel up to a temperature ratio of 9. They have noticed changes in the mean velocity, turbulent kinetic energy, mean temperature, and fluctuation temperature profiles. Nicoud [19, 20] has considered temperature ratios of 1.01, 2, and 4 with two kinds of law for the property variations. The temperature ratios of 1.01 and 2 are solved using an evolution of the property given for a gas flow, and another temperature ratio of 2 and one of 4 are done for an evolution given for a liquid flow. Nicoud observed significant modifications of the mean and turbulent profiles, in particular a dissymmetry, even with a semilocal scaling. His results also show that the intermittence seems to be enhanced close to the hot wall. Nevertheless, these studies consider only a low turbulent Reynolds number ($Re_{\tau m} \approx 180$). Our work using thermal large eddy simulation confirms these results for low turbulent Reynolds number ($Re_{\tau m} \approx 180$) and proposes new results for a higher turbulent Reynolds number ($Re_{\tau m} \approx 395$). Therefore, the present study is more global, complete, and systematic. The principal aim is to tend to the physical conditions of solar

Table 1 Summary of the large-eddy simulations carried out

Case	$Re_{\tau m}$	Re_b	T_2/T_1	λ, μ	Pr_{sgs}	Mesh resolution	Number of nodes
180-1.01-cc	180	2842	1.01	constant	constant	$\Delta x^+ \approx 35$	33 × 66 × 39
180-1.01-cd	180	2842	1.01	constant	dynamic	$\Delta z^+ \approx 15$	
180-2-vc	180	2362	2	variable	constant	$0.5\ \delta\ \Delta y^+ \leq 11$	In x, y and z directions
180-2-vd	180	2368	2	variable	dynamic		
395-1.07-vc	395	7494	1.07	constant	constant	$\Delta x^+ \approx 39$	64 × 65 × 32
395-1.07-vd	395	7329	1.07	variable	dynamic	$\Delta z^+ \approx 40$	
395-2-cc	395	6981	2	constant	constant		
395-2-vc	395	5853	2	variable	constant	$1\ \delta\ \Delta y^+ \leq 25$	In x, y and z directions
395-2-vd	395	5850	2	variable	dynamic		

receivers and to propose physical explanation of the coupling between turbulence and temperature gradient that could help future optimization of solar receivers.

After the presentation of the configuration, the governing equations, and the model validation, we discuss the influence of the viscosity and conductivity variations. We then investigate the difference between two thermal subgrid-scale models. The first one is based on a constant subgrid-scale Prantdtl number and the other one calculates dynamically the subgrid-scale Prandtl number. Afterward we compare the results of the high temperature ratio simulations ($T_2/T_1 = 2.00$) with those of the low temperature ratio simulations ($T_2/T_1 = 1.01$ and 1.07). Finally, we analyze the physical phenomenon that leads to the modifications on the mean and turbulent profiles when T_2/T_1 increases for average turbulent Reynolds numbers based on the friction velocity (Eqs. (18) and (22)) of 180 and 395.

GOVERNING EQUATIONS AND NUMERICAL SETUP

Thermal large eddy simulation is a very useful tool for thermal fluid mechanics problems [21] and it is well adapted to studying the flow in a solar receiver. It is more accurate than Reynolds averaged Navier–Stokes (RANS) methods for the study of turbulent flows [22] and, due to its "lower" computational cost, it permit consideration of more complicated configurations and higher Reynolds numbers than direct numerical simulation (DNS) does. In our case, it permits us to generate a database. Furthermore, the real time for one thermal large eddy simulation is already expensive. We make a parametric study for a given turbulent Reynolds number. We compare simulations with the same turbulent Reynolds number ($Re_{\tau m}$) for different temperature ratios. Finally, we have to find the good flow rate to obtain the target turbulent Reynolds number. None of the tested correlations permits us to find the good flow rate. So we have to iterate on the flow rate value (three to six iterations are necessary) to reach the target turbulent Reynolds number. Consequently, the choice of thermal large eddy simulation imposes itself as the best solution.

Governing Equations

This article is concerned with a low Mach number flow of an ideal gas subjected to significant heat transfer causing important fluids properties variations. In particular, the density variations cannot be neglected in the continuity equation: The incompressibility constraint is false. However, acoustic waves do not interact with the flow. Therefore, we used an algorithm based on the low Mach number equations. In doing so, the density is decoupled from the pressure so that no acoustics are present in the computation. To obtain this particular set of equations, the compressible mass, momentum, and energy balance equations are transformed using the fact that the Mach number is very small [7]. This method can be applied to ideal gas flows with a Mach number lower than 0.3, without any restriction on the temperature variations. In this study, the gas considered is air.

Thermal large eddy simulation is based on a spatial filtering, noted by $(-)$, to separate the large scales from the small scales. This filtering uses Favre averaging:

$$\tilde{\Phi} = \frac{\overline{\rho \Phi}}{\bar{\rho}} \tag{1}$$

The Favre filtered low-Mach equations (2) to (6) in thermal large eddy simulation modeling are the following [23]:

$$\left\{\begin{aligned}
&\frac{\partial \bar{\rho}}{\partial t} + \frac{\partial\left(\bar{\rho}\tilde{U}_j\right)}{\partial x_j} = 0 && (2)\\
&\frac{\partial \bar{\rho}\tilde{U}_i}{\partial t} + \frac{\partial\left(\bar{\rho}\tilde{U}_i\tilde{U}_j\right)}{\partial x_j} = \frac{\partial \bar{P}'}{\partial x_i} + \frac{\partial}{\partial x_j}\left[\bar{\mu}\left(\frac{\partial \tilde{U}_i}{\partial x_j} + \frac{\partial \tilde{U}_j}{\partial x_i}\right)\right] &&\\
&\quad -\frac{2}{3}\frac{\partial}{\partial x_i}\left(\bar{\mu}\frac{\partial \tilde{U}_j}{\partial x_j}\right) - \frac{\partial \tilde{U}_{ij}}{\partial x_j} && (3)\\
&Cp\left(\frac{\partial\left(\bar{\rho}\tilde{T}\right)}{\partial t} + \frac{\partial\left(\bar{\rho}\tilde{U}_i\tilde{U}_j\right)}{\partial t}\right) = \frac{\partial \bar{P}_{\text{thermo}}}{\partial t} + \frac{\partial}{\partial x_j}\left(\bar{\lambda}\frac{\partial \tilde{T}}{\partial x_j}\right) &&\\
&\quad -\frac{\partial \Im_j}{\partial x_j} && (4)\\
&\bar{P}_{\text{thermo}} = \bar{\rho}R\tilde{T} && (5)\\
&\frac{\partial \bar{P}_{\text{thermo}}}{\partial x_i} = 0 && (6)
\end{aligned}\right.$$

In this set of equations, ρ is the density, U_i are the velocity components, T is the temperature, t represents the time, x_i are the coordinates, λ and μ are the conductivity and the dynamic viscosity, C_P is the constant pressure heat capacity, P' is the corrected dynamic pressure, and P_{thermo} is the thermodynamic pressure. The two unknown terms that appear in Eqs. (3) and (4) due to the filtering operation are the subgrid-scale tensor, τ_{ij}, and the subgrid-scale heat flux, $\Im_j$. They are defined as:

$$\left|\begin{aligned}
&\tau_{ij} = \bar{\pi}\left(\widetilde{U_i U_j} - \tilde{U}_i\tilde{U}_j\right) && (7)\\
&\Im_j = \bar{\rho}Cp\left(\widetilde{TU_j} - \tilde{T}\tilde{U}_j\right) && (8)
\end{aligned}\right.$$

Subgrid-scale models must be used to represent these terms and therefore allow the numerical resolution. To that aim, we use a subgrid-scale kinetic viscosity νsgs:

$$\left|\tau_{ij} - \frac{1}{3}\delta_{ij}\tau\kappa\kappa = -2\bar{\rho}\nu_{sgs}\tilde{S}_{ij}\right. \tag{9}$$

where δ_{ij} is the Kronecker symbol and S_{ij} is the strain tensor:

$$\left|\tilde{S}_{ij} = \frac{1}{2}\left(\frac{\partial \tilde{U}_i}{\partial x_j} + \frac{\partial \tilde{U}_j}{\partial x_i}\right)\right. \tag{10}$$

The isotropic part (τ_{kk}) of the subgrid-scale tensor is not modelized. It is simply added to the dynamic pressure in Eq. (3):

$$\bar{P}' = \bar{P}_{dyn} + \frac{1}{3}\tau kk \tag{11}$$

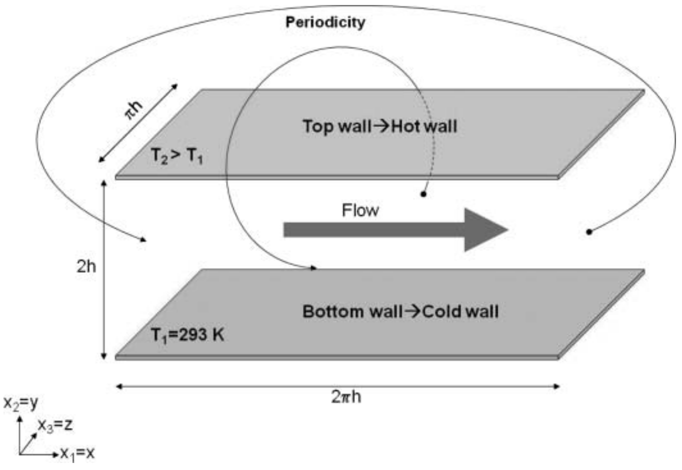

Figure 2 Studied configuration.

This is possible because the dynamic and the thermodynamic pressure are decoupled. The dynamic pressure is calculated by solving the mass conservation. The time variation of the thermodynamic pressure is evaluated by using the ideal gas law [24]. For the subgrid-scale heat flux, $\Im_j$ we use a subgrid-scale diffusivity κsgs:

$$\Im_j = -\bar{\rho} C p \kappa_{\mathrm{sgs}} \frac{\partial \tilde{T}}{\partial x_j} \tag{12}$$

The subgrid-scale thermal diffusivity can then be expressed as a function of the subgrid-scale kinematic viscosity:

$$\kappa_{\mathrm{sgs}} = \frac{\upsilon_{\mathrm{sgs}}}{P\tau_{\mathrm{sgs}}} \tag{13}$$

where $\mathrm{Pr}_{\mathrm{sgs}}$ is the subgrid-scale Prandtl number.

To express the subgrid-scale viscosity, we employ the Wale model developed by Nicoud and Ducros [25]. This model is based on both the strain and the rotation tensor and reproduces correctly the asymptotic behavior of the eddy viscosity at the wall ($\nu_{\mathrm{sgs}} \propto y^3$). The constant of this model is set to $C\omega = 0.5$, as recommended by the authors [25].

For the subgrid-scale diffusivity, we test two methods:

- A constant subgrid-scale Prandtl number (Prsgs = 0.9 suggested by Nicoud and Poinsot [26] in our configuration). Other studies [5, 13, 27] consider a constant value equal to 0.6. The higher value (0.9 instead of 0.6) seems a posteriori correct by comparison with the dynamics Prandtl number (Figures 9 and 11a).
- The dynamic calculation of the subgrid-scale Prandtl number proposed by Moin et al. [27].

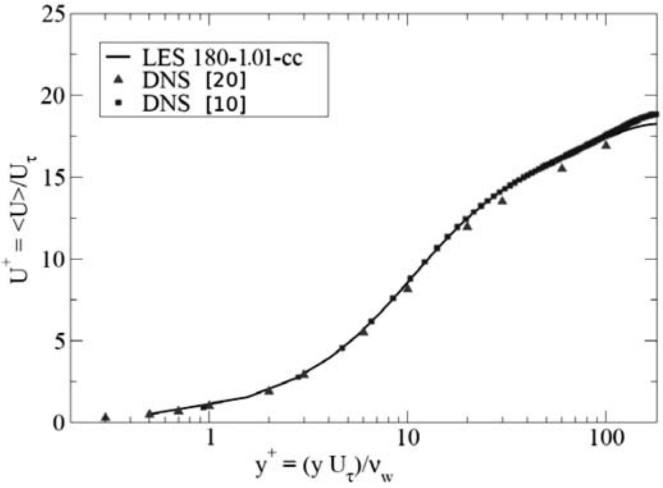

(a) Longitudinal mean velocity

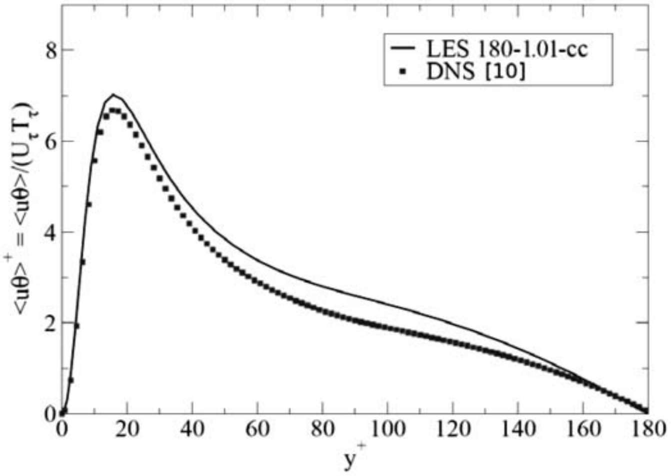

(b) Longitudinal velocity-temperature correlation

Figure 3 Validation with the DNS data.

The conductivity λ and the dynamic viscosity μ are solved using the Sutherland law:

$$\mu\,(T) = 1.461.10^{-6} \frac{T^{1.5}}{T + 111} \tag{14}$$

$$\lambda\,(T) = \frac{\mu C p}{\mathrm{P}\tau} = \frac{1.468.10^{-3}}{P\tau} \frac{T^{1.5}}{T + 111} \tag{15}$$

Some simulations are realized using the hypothesis that the conductivity and the dynamic viscosity can be considered as a constant. In that case, the properties are evaluated in function of the average temperature, obtained by the mean value between the two walls temperatures $T_m = (T_1 + T_2)/2$, using Eqs. (14) and (15).

For the isothermal simulation, the density is considered as a constant. Nevertheless, for the simulations using the low Mach number hypothesis, the density is solved using the ideal gas law

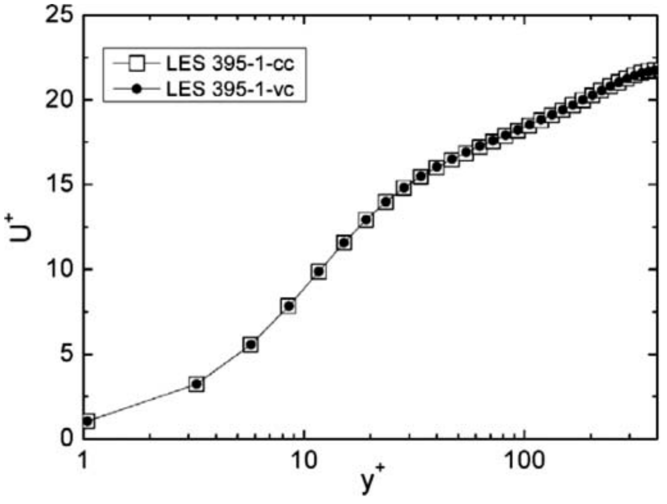

(a) Mean longitudinal velocity

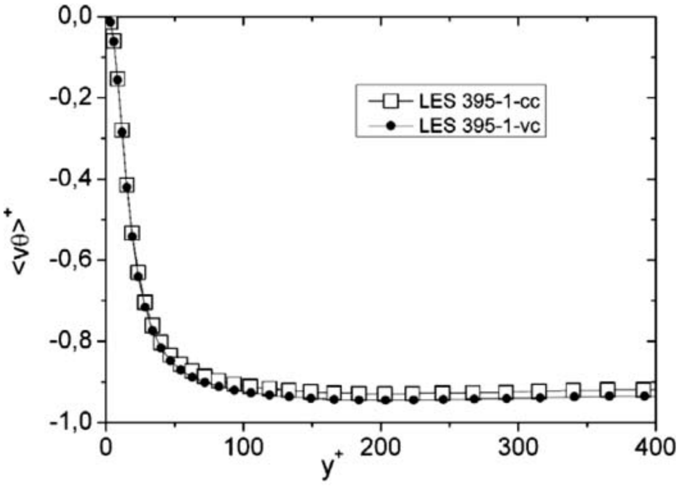

(b) Vertical velocity - temperature correlation.

Figure 4 Influence of λ and μ for $T_2/T_1 = 1.07$ at $Re_{\tau m} = 395$.

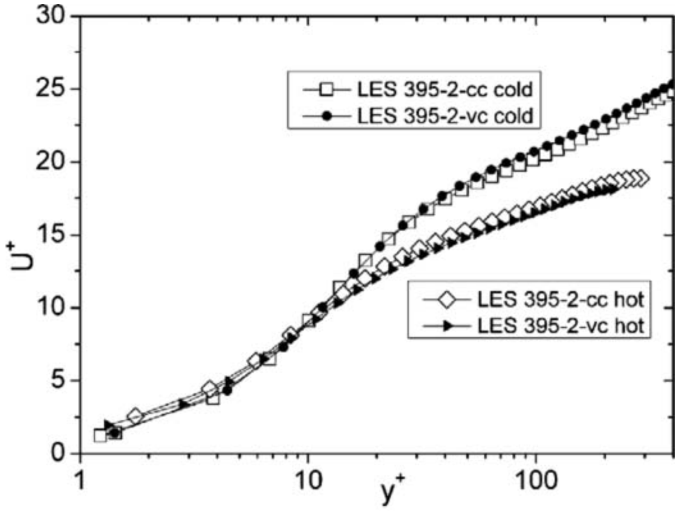

(a) Mean longitudinal velocity.

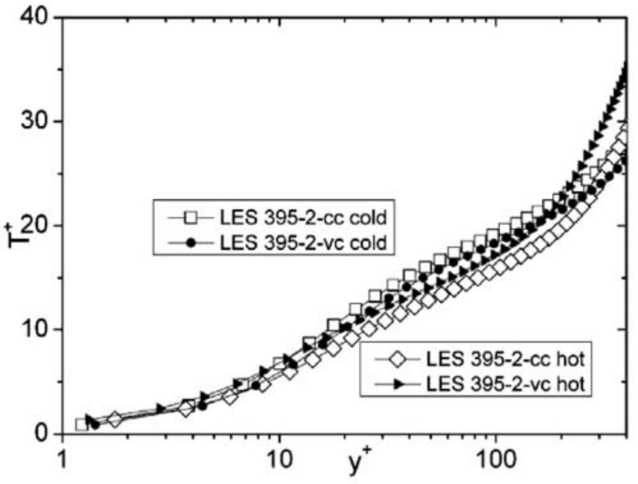

(b) Mean temperature.

Figure 5 Influence of λ and μ for $T_2/T_1 = 2.00$ at $Re_{\tau m} = 395$: mean velocity and temperature.

$\rho = \frac{P_{thermo}}{RT}$ where $P_{thermo} = 1.10^{-5}$ Pa and R is the ideal gas specific constant.

The calorific capacity $Cp = 1005$ J kg^{-1} K^{-1}. For the simulations at $Re_{\tau m} = 395$ we chose a Prandtl number of 0.71 and for the simulations at $Re_{\tau m} = 180$ we chose $Pr = 0.76$ as indicated by Nicoud [20] and Nicoud and Poinsot [26] in their DNS.

Numerical Setup

We study the turbulent air flow in an horizontal plane channel with imposed temperatures at the walls (Figure 2). The channel length are $2\pi h \times 2h \times \pi h$ (with $h = 0.014923$ m), following the conclusions of previous works [28, 29]. The lower plate is the cold one and the upper plate is the hot one. In the following, the subscript 1 refers to the bottom wall (cold) and the subscript 2 is related to the top wall (hot). As shown in Figure 2, the longitudinal axis, x_1, corresponds to the flow direction, the vertical axis, x_2, is normal to the walls, and the last axis, x_3, is in the transverse direction.

Simulations are carried out with the Trio U code developed at the CEA (French Atomic Agency). To solve a fully developed flow, we use a periodic boundary condition in the streamwise and the spanwise directions. All the simulations assume a constant mass flux. For the wall boundary condition, we use constant temperature and no slip condition. The temperature at the lower wall T_1 is fixed at 293K in all the simulations.

Time integration is carried out by a third-order Runge–Kutta scheme. The convection scheme for the velocity is a second-order centered scheme ([30]). For the temperature, we use a third-order quick scheme, as recommended by Chatelain et al. [31] and Brillant et al. [30].

The statistics are done by averaging in space in the two periodic directions and in time. The spatial averaging operator

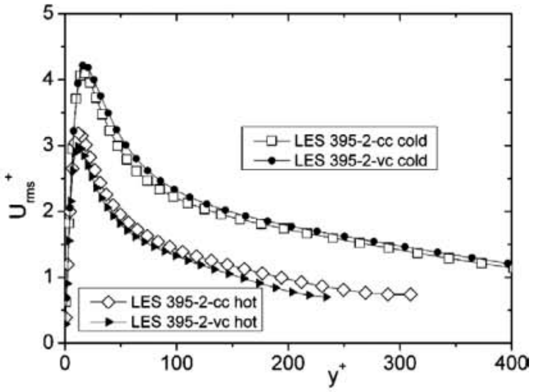

(a) Longitudinal velocity fluctuations.

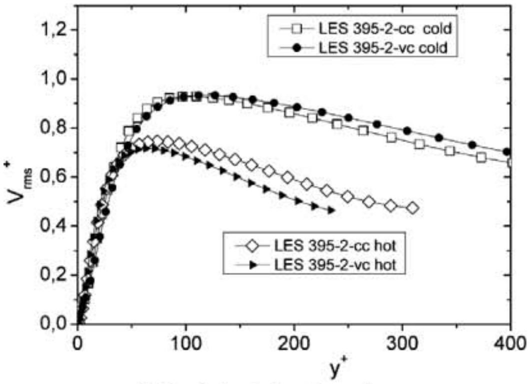

(b) Vertical velocity fluctuations.

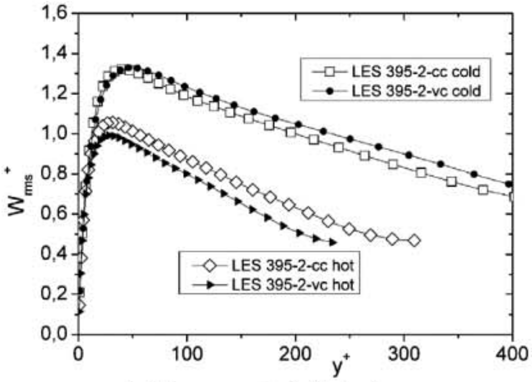

(c) Transverse velocity fluctuations.

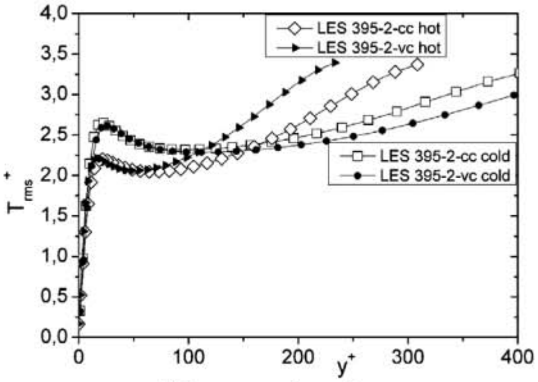

(d) Temperature fluctuations.

Figure 6 Influence of λ and μ for $T_2/T_1 = 2.00$ at $Re_{\tau m} = 395$: velocity and temperature fluctuations.

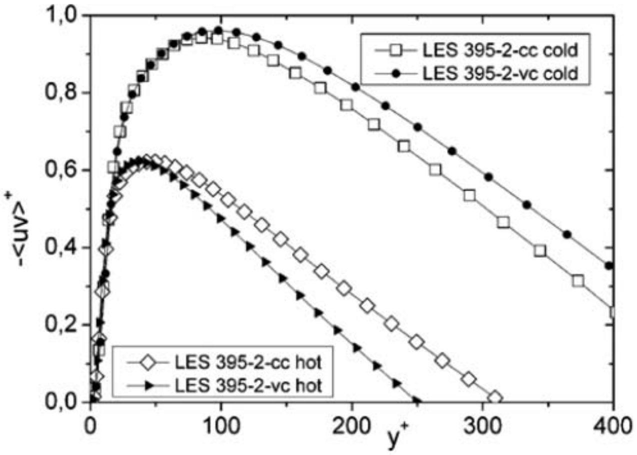

(a) Longitudinal velocity - vertical velocity correlation.

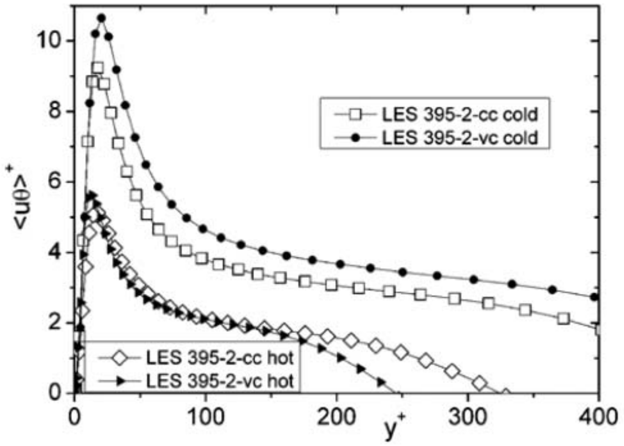

(b) Longitudinal velocity - temperature correlation.

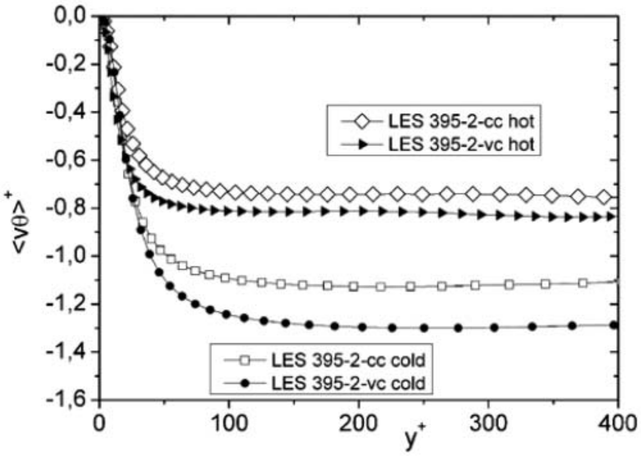

(c) Vertical velocity - temperature correlation.

Figure 7 Influence of λ and μ for $T_2/T_1 = 2.00$ at $Re_{\tau m} = 395$: correlations.

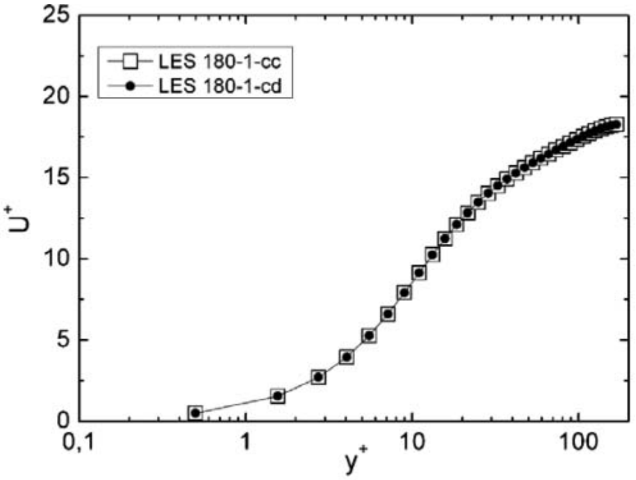

(a) Mean longitudinal velocity.

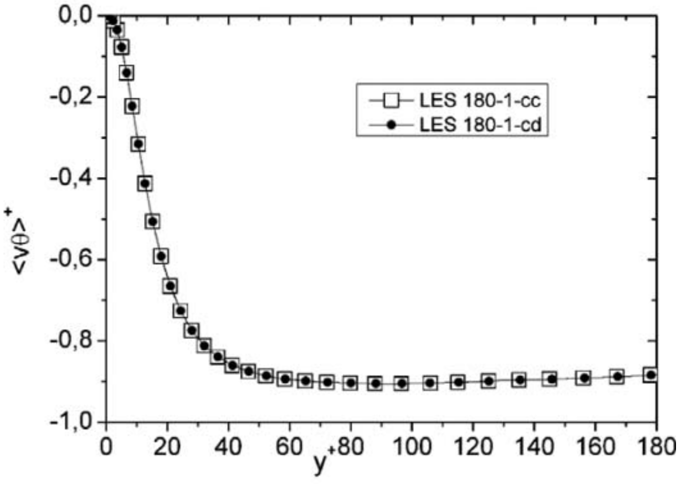

(b) Vertical velocity - temperature correlation.

Figure 8 Influence of the thermal subgrid-scale model for $T_2/T_1 = 1.01$ at $Re_{\tau m} = 180$.

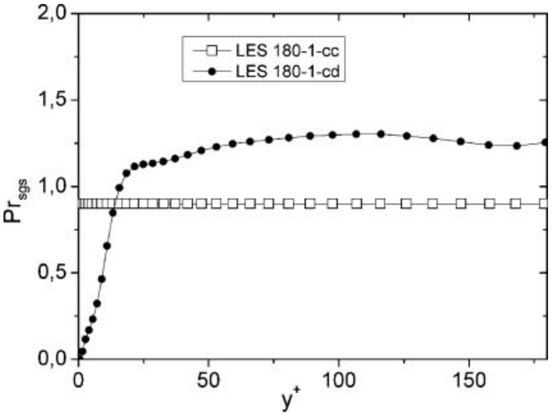

Figure 9 Evolution of the subgrid-scale Prandtl number for $T_2/T_1 = 1.01$ at $Re_{\tau m} = 180$.

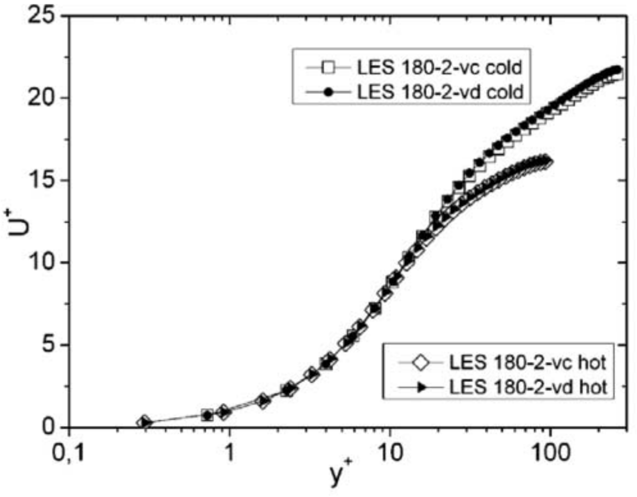

(a) Mean longitudinal velocity.

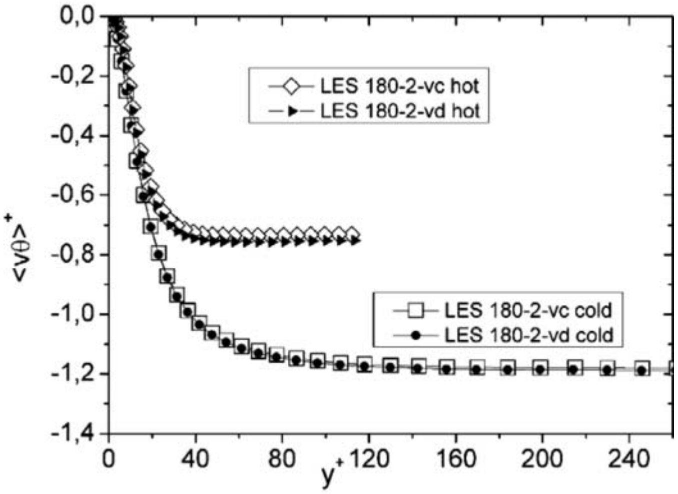

(b) Vertical velocity - temperature correlation.

Figure 10 Influence of the thermal subgrid-scale model for $T_2/T_1 = 2.00$ at $Re_{\tau m} = 180$.

$\ll . \gg$ is given by:

$$\ll f(y,t) \gg$$

$$= \frac{1}{2\pi h}\int_{x=0}^{x=2\pi h}\left(\frac{1}{\pi h}\int_{z=0}^{z=\pi h} f(x,y,z,t)\,dz\right)dx \quad (16)$$

The time averaging operator $<.>$ is:

$$<f>(y) = \lim_{t_f->\infty}\frac{1}{t_f}\int_{t_0}^{t_0+t_f} \ll f(y,t) \gg dt \quad (17)$$

It permits us to obtain the mean quantities used in this article:

- The mean longitudinal velocity $<\tilde{U}>$.
- The mean temperature $<\tilde{T}>$.
- The longitudinal velocity fluctuations $< U_{rms} >= \sqrt{<\tilde{U}\tilde{U}> - <\tilde{U}><\tilde{U}>}$.

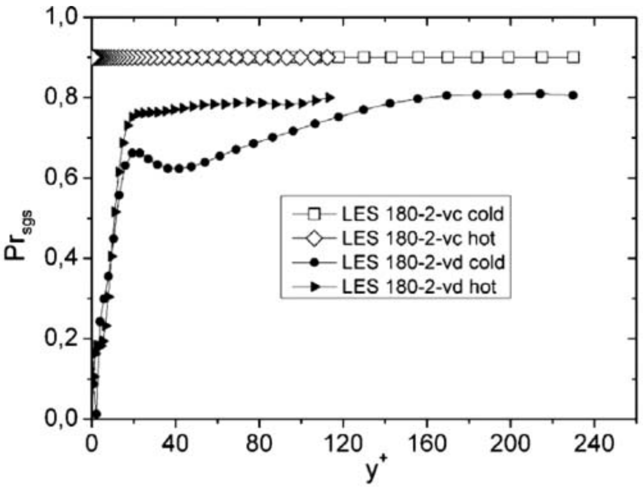

(a) Subgrid-scale Prandtl number

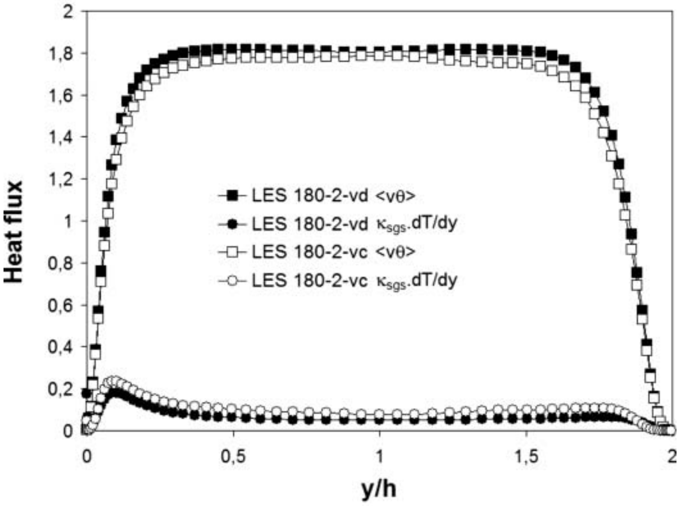

(b) Resolved and modeled turbulent heat flux.

Figure 11 Simulations at $Re_{\tau m} = 180$ for $T_2/T_1 = 2.00$.

- The vertical velocity fluctuations $< V_{rms} >= \sqrt{<\tilde{V}\tilde{V}> - <\tilde{V}><\tilde{V}>}$.
- The transverse velocity fluctuations $< W_{rms} >= \sqrt{<\tilde{W}\tilde{W}> - <\tilde{W}><\tilde{W}>}$.
- The temperature fluctuations $< T_{rms} >= \sqrt{<\tilde{T}\tilde{T}> - <\tilde{T}><\tilde{T}>}$.
- The longitudinal - vertical velocity correlation $< uv >=< \tilde{U}\tilde{V} > - < \tilde{U} >< \tilde{V} >$.
- The longitudinal velocity - temperature correlation $< u\theta >=< \tilde{U}\tilde{T} > - < \tilde{U} >< \tilde{T} >$.
- The vertical velocity - temperature correlation $< v\theta >=< \tilde{V}\tilde{T} > - < \tilde{V} >< \tilde{T} >$.

For the characterization of our simulations, we use the friction velocity U_τ that is solved with the near wall mean velocity gradient,

$$U_\tau = \sqrt{\frac{\tau_w}{\rho_w}} = \sqrt{\nu_w \left.\frac{\partial < \tilde{U} >}{\delta y}\right|_w} \tag{18}$$

where the subscript ω refers to wall quantities: ω → 1 on the bottom side and ω → 2 on the top side; τ_ω is the wall shear stress, ρ_ω and ν_ω are the density and the viscosity at the wall, and $\left.\frac{\partial<\tilde{U}>}{\delta y}\right|_w$ is the mean velocity gradient at the wall.

We plot the profiles as a function of y+ that is defined as:

$$y^+ = \frac{yU_\tau}{\nu_w} \tag{19}$$

Two temperatures are also considered:

- The average temperature:

$$T_m = \frac{T_1 + T_2}{2} \tag{20}$$

- The friction temperature:

$$T_\tau = \frac{Q_w}{\rho_w C_P U_\tau} = \frac{\lambda_w \left.\frac{\partial \tilde{T}}{\partial y}\right|_w}{\rho_w C_P U_\tau} \tag{21}$$

where Q_w is the heat flux at the wall.

This friction velocity and friction temperature are used to calculate the dimensionless profiles:

$$U^+ = \frac{< \tilde{U} >}{U_\tau}, \quad U^+_{rms} = \frac{< U_{rms} >}{U_\tau}, \quad V^+_{rms} = \frac{< V_{rms} >}{U_\tau},$$
$$W^+_{rms} = \frac{< W_{rms} >}{U_\tau}, \quad T^+ = \frac{< \tilde{T} > - T_w}{T_\tau} T^+_{rms} = \frac{< T_{rms} >}{T_\tau},$$
$$< uv >^+ = \frac{< uv >}{U_\tau^2}, \quad < u\theta >^+ = \frac{< u\theta >}{U_\tau T_t},$$
$$< v\theta >^+ = \frac{<v\theta>}{U_\tau T_t}$$

The profiles on the cold side are normalized using $U_{\tau 1}$ and $T_{\tau 1}$ and the profiles on the hot side are normalized using $U_{\tau 2}$ and $T_{\tau 2}$.

The turbulent Reynolds number Re_τ is based on the friction velocity and the viscosity at the wall:

$$Re_\tau = \frac{U_\tau h}{\nu_w} \tag{22}$$

For this study we have to distinguish three different turbulent Reynolds numbers:

- $Re_{\tau 1}$ is calculated at the upper wall (hot one).
- $Re_{\tau 2}$ is calculated at the lower wall (cold one).
- $Re_{\tau m}$ is the average value between Reτ1 and Reτ2 $\left(Re_{\tau m} = \frac{Re_{\tau 1} + Re_{\tau 2}}{2}\right)$.

For this work, the target turbulent Reynolds numbers chosen for the comparisons are the averaged values ($Re_{\tau m}$: 180 and 395).

Table 2 Turbulent Reynolds numbers, friction velocities, and friction temperatures of the large-eddy simulations carried out

Case	$\mathrm{Re}_{\tau m}$	$\mathrm{Re}_{\tau 1}$	$\mathrm{Re}_{\tau 2}$	$\mathrm{U}_{\tau 1}$	$\mathrm{U}_{\tau 2}$	$\mathrm{T}_{\tau 1}$	$\mathrm{T}_{\tau 2}{}^{\sim}$
180-1.01-cc	179	179	178	0.184	0.185	0.0635	0.0637
180-1.01-cd	179	179	179	0.184	0.185	0.0635	0.0637
180-2-vc	184	262	106	0.268	0.355	5.762	6.937
180-2-vd	184	261	107	0.267	0.358	5.749	6.693
395-1.07-vc	396	404	388	0.423	0.435	0.355	0.348
395-1.07-vd	390	405	375	0.414	0.430	0.355	0.350
395-2-cc	398	477	320	0.658	0.881	5.160	5.056
395-2-vc	396	551	241	0.563	0.809	5.216	5.025
395-2-vd	398	554	242	0.566	0.812	5.253	4.797

In Table 1, the bulk Reynolds number is calculated as following:

$$\mathrm{Re}_b = \frac{U_b h}{\nu_b} \tag{23}$$

with

$$U_b = \frac{1}{2h}\int_0^{2h} < \tilde{U} > (y)dy \tag{24}$$

and ν_b obtained with the bulk temperature T_b:

$$T_b = \frac{1}{2h}\int_0^{2h} < \tilde{T} > (y)dy \tag{25}$$

With an average turbulent Reynolds number based on the friction velocity of $\mathrm{Re}_{\tau m} = 395$, the computational cost is higher but we ensure avoiding low Reynolds number effects; the time step for the simulation of weakly non-isothermal and turbulent flow is $\Delta t \approx 1\ 10^{-4}$ s, and for the same temperature but with a high turbulent intensity, it is $\Delta t \approx 4\ 10^{-5}$ s. These effects can appear at the top wall, where the temperature is high, and the viscosity tends to laminarize the flow if the average turbulent Reynolds number is not high enough [11, 20]. Indeed, as can be seen in Table 2, in our thermal large eddy simulation for $\mathrm{Re}_{\tau m} \approx 180$ and a temperature ratio $\mathrm{T}_2/\mathrm{T}_1 = 2.00$, the turbulent Reynolds number is much higher than 180 at the lower wall and decreases down to about 106 at the upper wall. With a mean $\mathrm{Re}_{\tau m} \approx 395$, even if the value of $\mathrm{Re}_{\tau 2}$ at the hot wall is reduced for high temperature ratios, the flow remains turbulent ($\mathrm{Re}_{\tau 2} > 240$).

We use two different meshes depending on the $\mathrm{Re}_{\tau m}$ considered. The first one has 84,942 nodes (for $\mathrm{Re}_{\tau m} = 180$) and the second one 133,120 nodes (for $\mathrm{Re}_{\tau m} = 395$). In the two cases, a uniform mesh is used in the directions x and z and a nonuniform mesh is used in the y direction (Table 1). The mesh is refined near the wall in order to obtain $\Delta y^+ \leq 1$ in all the simulations.

The designations of the simulations carried out in this study and their main parameters are summarized in Tables 1 and 2. The friction velocities and temperatures given in Table 2 are used to normalize the profiles displayed in the following sections.

The time step of the computation decreases with the increase of the turbulent Reynolds number and of the temperature ratio. It varies between $\Delta t \approx 1\ 10^{-4}$ s, for the isothermal simulation with a weak turbulent intensity, to $\Delta t \approx 8\ 10^{-6}$ s for the most turbulent simulation with a temperature ratio of two. Furthermore, the time needed to converge the temporal averaging increases with the turbulent Reynolds number and the temperature ratio. For the isothermal simulation at $\mathrm{Re}_{\tau m} = 180$, in terms of diffusion time (h/Uτ here equal to 0.08 s) we need to collect data over 25 diffusion time. When the turbulent Reynolds number and the temperature ratio increase (for example the simulation 395-2), the diffusion time is equal to 0.014 s and we need more over 30 diffusion time to converge data. Finally, the time for one simulation varies from 2 months to 6 months on 16 processors.

Validation

Our simulations have been validated by comparisons with DNS in the weakly non-isothermal and turbulent cases. This is done assuming that LES quantities ($\tilde{U}$ and $\tilde{T}$) can be directly compared to DNS quantities (u and T) [5, 6, 11, 12, 15, 18, 32–35]. At $\mathrm{Re}_{\tau m} = 180$, we compared an isothermal LES with the DNS of Kim et al. [36], a weakly non-isothermal thermal large eddy simulation ($\mathrm{T}_2/\mathrm{T}_1 = 1.01$) with the DNS of Nicoud [20] and Debusschere and Rutland [10], and a strongly non-isothermal thermal large eddy simulation ($\mathrm{T}_2/\mathrm{T}_1 = 2$) with the DNS carried out by Nicoud [20]. At $\mathrm{Re}_{\tau m} = 395$, we compared an isothermal LES with the DNS of Moser et al. [37] and Kawamura et al. [38]. To our knowledge, there do not exist any DNS or LES data for a non-isothermal simulation at $\mathrm{Re}_{\tau m} = 395$.

For all the simulations where DNS data are available (Table 3), we obtained a fair agreement between our simulations and the reference DNS data for the mean, fluctuation and correlation profiles. For example, in Figure 3, we can see the comparison, for the longitudinal mean velocity and the velocity–temperature correlation, for the simulation weakly non-isothermal at $\mathrm{Re}_{\tau m} = 180$.

We know that a finer mesh in the transverse direction would permit us to perfectly fit the DNS profiles, as it has been observed by Chatelain et al. [31] with the same configuration and the same code than in the present study. When the authors increase the number of nodes, the LES results match the DNS data. However, the corresponding thermal large eddy simulation would not converge within a reasonable time and therefore such a mesh would not allow us to carry out several simulations with a high temperature ratio. For an isothermal simulation at $\mathrm{Re}_{\tau m} = 395$, the time step varies from $\Delta t \approx 5\ 10^{-5}$ s, with our mesh, to $\Delta t \approx 3\ 10^{-5}$ s, with a finer mesh (that represents always a thermal large eddy simulation and not a DNS). This increase is too important for an isothermal case, knowing that the impact of the temperature gradient strongly decreases the time step and makes it too small for our study.

IMPACT OF FLUID PROPERTY VARIATIONS

In this study, the selected equations permit us to take into account the density variations, whereas the viscosity and the conductivity can either be constant or vary with the temperature according to given laws (Sutherland's law in the present study). When the variations of these properties are considered, we expect the results to be more accurate but the calculation cost increases significantly when the temperature of the upper wall is high. The choice between constant and varying conductivity and viscosity is therefore questionable. For this study, all the simulations are realized considering a constant subgrid-scale Prandtl number.

To determine whether λ and μ can be considered constant, we compare, for a low and a high temperature ratio, the results obtained when the conductivity and the viscosity vary with those given by simulations where λ and μ are fixed (values taken at the average temperature $\mathrm{T_m}$).

Low temperature ratio: $\frac{T_2}{T_1} = 1.07$

In this section, we compared the simulations 395-1.07-cc and 395-1.07-vc.

The profiles of the mean velocity and temperature as well as of the velocity and temperature fluctuations are identical for the two simulations. For example, we can see in Figure 4a the mean longitudinal velocity. The main differences are obtained for the velocity–temperature correlation, particularly for the vertical velocity–temperature correlation (Figure 4b).

The good agreement between the profiles of both simulations leads us to the conclusion that the variations of λ and μ are negligible for a low temperature ratio, as suggested by the small values of relative error (3%) obtained on the conductivity and on the viscosity between the two simulations.

High temperature ratio: $\frac{T_2}{T_1} = 2$

In this section, we compared the simulations 395-2-cc and 395-2-vc. The profiles of this case are compared in Figures 5, 6, and 7. Since the curves of both halves of the channel do not collapse for such a high temperature ratio, the profiles at the bottom (cold) wall and at the top (hot) wall are displayed separately.

The mean velocity profiles obtained with constant and varying λ and μ well agree in the linear region both on the cold and the hot sides of the channel (Figure 5a). In the logarithmic region, they are less close to each other. However, the difference is too small to be significant. In Figure 5b, we can see that for the mean temperature profiles, neglecting the variations of the conductivity and the viscosity leads to keeping away the profiles obtained near the cold and the hot walls and to bringing them together in the channel centerline.

The longitudinal, vertical, and transverse velocity fluctuations are shown in Figures 6a–c. On these three plots, we observe discrepancies between cases 395-2-cc and 395-2-vc. Considering λ and μ constant induces an overestimation of the velocity fluctuations level on the hot half of the domain and an underestimation of their level on the cold half. For the longitudinal velocity fluctuation, the profiles related to both simulations differ only slightly. For the vertical and transverse velocity fluctuations, the gap between the curves of simulations 395-2-cc and 395-2-vc is more marked. In particular, we note that this deviation increases as we get further away from the walls, and the maximum gap between the profiles of the two cases is obtained in the central region of the channel, closer to the hot side. This result is surprising because the variations of λ and μ are important where the variations of temperature are important (near the wall). In fact, the variations of the mean temperature do not seem to have an effect: These variations are big near the wall $\left(\frac{\partial <\tilde{T}>}{\partial y} \Big\|_w \gg 1 \right)$ but the profiles are not modified at this place. On the contrary, the fluctuations of temperature (Trms) seem to have an important effect: These fluctuations are maximum in the center of the channel, where the maximum difference between the profiles is observed. When the variations of the conductivity and the viscosity are neglected, another modification of the profiles appears in Figures 6a–c: The peak locations are slightly shifted.

For the temperature fluctuations, we observe in Figure 6d that the profiles given by thermal large eddy simulations 395-2-cc and 395-2-vc are very close in the near-wall area ($\mathrm{y}^+ \leq 60$). Then they deviate and the gap increases toward the channel centerline, both on the cold side and on the hot side. Neglecting the variations of the conductivity and the viscosity induces an underestimation of Trms in the hot half of the domain and an overestimation in its cold half (effect opposite that for the velocity fluctuations). However, we can note that for all the profiles of the fluctuations (velocity and temperature), we have to take into account the effect of the temperature on the viscosity and the conductivity.

From Figure 7a, it can be clearly stated that using fixed values for λ and μ instead of taking their variations into account causes significant discrepancies in the velocity–velocity correlation profiles. Close to the wall, there is no visible difference

Table 3 DNS used for validation

$\frac{T_2}{T_1} =$	$\mathrm{Re}_\tau = 180$	$\mathrm{Re}_\tau = 395$
1	Kim et al. [36]	Moser et al. [37], Kawamura et al. [38]
1.01	Debusschere & Rutland [10], Nicoud [20]	
2	Nicoud [20]	

between the two cases. But after the peak, the profiles deviate more and more as the channel centerline gets closer. For the velocity–velocity correlation <uv>, the simulation with constant viscosity and conductivity, by comparison to the simulation taking into account the property variations, leads to a much lower profile on the cold side of the domain and to a much higher profile on the hot side. We note, however, an overestimation of <vθ> on the cold half of the channel (Figure 7), as well as a distinct overestimation of <uθ> in the center of the domain on the hot side when the variations of λ and μ are neglected.

For $T_2/T_1 = 2.00$ there are significant differences between the results obtained when the conductivity and the viscosity are constant and the results when they vary with the temperature. For the high temperature ratio, the variations of λ and μ cannot be neglected. Furthermore, the effect of dissymmetry due to the temperature gradient increases when we take into account the variation of the viscosity and of the conductivity.

As a conclusion, for the lower temperature ratio, we show that the impact of the variations of these properties is negligible since the relative errors on the viscosity and the conductivity are smaller than 3% $\left(\text{relative error}: Max\left(\frac{\mu_1-\mu_m}{\mu_m}, \frac{\mu_m-\mu_2}{\mu_m}\right) \text{ and } Max\left(\frac{\lambda_1-\lambda_m}{\lambda_m}, \frac{\lambda_m-\lambda_2}{\lambda_m}\right)\right)$. For the higher temperature ratio, the relative error reaches about 24%. Therefore, their impacts should not be neglected anymore.

STUDY OF THERMAL SUBGRID-SCALE MODELING

The models that can be most properly employed in thermal large eddy simulation to represent the subgrid-scale heat flux are the model based on a constant subgrid-scale Prandtl number and the model consisting of a dynamic calculation of Pr_{sgs} developed by Moin et al. [27]. The advantage of the first of these models is its simplicity. However, it relies on the assumption that the temperature field behavior is similar to the velocity field behavior, which has no reason to hold as the temperature gradient increases. The dynamic model of Moin et al. [27] seems more appropriate to the study of non-isothermal flows but is more complex and decreases the time step. We intend here to compare both models for low and high temperature ratios to find out whether assuming a constant subgrid-scale Prandtl number has an impact or not in our configuration in weakly and strongly non-isothermal cases.

Low Temperature Ratio

We carried out two simulations, weakly non-isothermal and with a weak turbulent intensity ($Re_{\tau m} \approx 180$ and $T_2/T_1 = 1.01$), that differ only on the model used for the subgrid-scale Prandtl number (180-1.01-cc and 180-1.01-cd). For all the mean, fluctuation, and correlation profiles, there is no difference between the two simulations. For example, we can see in Figure 8a the longitudinal mean velocity, and in Figure 8b, the vertical velocity–temperature correlation, and we can note that the curves fit very well. This result is not evident if we are looking at the evolution of the subgrid-scale Prandtl number (Figure 9).

In conclusion, for a weak temperature gradient, the model based on a constant Pr_{sgs} is therefore suitable. This conclusion is in agreement with the work of Brillant et al. [39], who also studied the thermal subgrid-scale modeling for the weakly non-isothermal turbulent channel flow.

High Temperature Ratio

We now consider strongly non-isothermal cases, $T_2/T_1 = 2.00$, $Re_{\tau m} = 180$, variable λ and μ, and compare the profiles obtained when the subgrid-scale Prandtl number is constant (simulation 180-2-vc) and dynamically calculated (simulation 180-2-vd). As previously mentioned, we need to distinguish the curves of the bottom and top halves of the channel since they are different for high temperature ratio. For all the mean, fluctuation, and correlation profiles, there are few differences between the two simulations. For example, we can see that the curves fit very well in Figure 10a for the longitudinal mean velocity and in Figure 10b for the vertical velocity–temperature correlation. This result was, again, not evident if we were looking at the evolution of the subgrid-scale Prandtl number (Figure 11a). However, we can see in Figure 11b, that in both cases, the resolved part of the turbulent heat flux is much more important than the modeled part. The simulation 180-2-vc increases the modeled part and decreases the resolved part by comparison to the simulation 180-2-vd. Thus, the total conductive flux (molecular and subgrid) is conserved. This could explain why the thermal subgrid-scale modelization does not affect the results between the two simulations.

As a conclusion, the comparison of cases 180-2-vc and 180-2-vd shows no major differences between the results obtained with the two thermal subgrid-scale models. There are some deviations but they are not distinct enough to question the similarity of the model based on a constant subgrid-scale Prandtl number and the model consisting of a dynamic calculation of Pr_{sgs} for $T_2/T_1 = 2.00$.

This similarity at a high temperature ratio is surprising. It might be due to the low turbulent Reynolds number considered here ($Re_{\tau m} = 180$), or to our mesh, which could be fine enough to prevent the thermal subgrid-scale model from having any influence. To check these hypotheses, we carried out additional simulations with $Re_{\tau m} = 395$ at temperature ratio of 2.

Inn Figures 12a and b, we can see that, as for the case at $Re_{\tau m} = 180$, it is not necessary to use a Pr_{sgs} solved dynamically. There are no significant differences between, the mean, fluctuation, and correlation profiles obtained with a constant or dynamic Pr_{sgs}.

We can conclude that, for a temperature ratio lower than or equal to 2, we can use a constant Pr_{sgs} to solve the thermal subgrid scale.

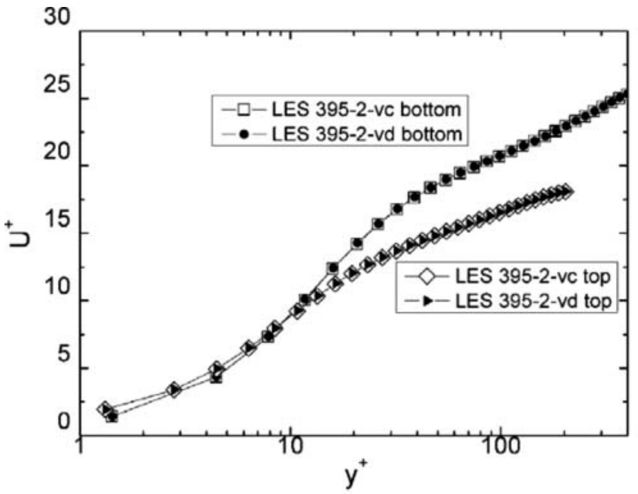

(a) Mean longitudinal velocity.

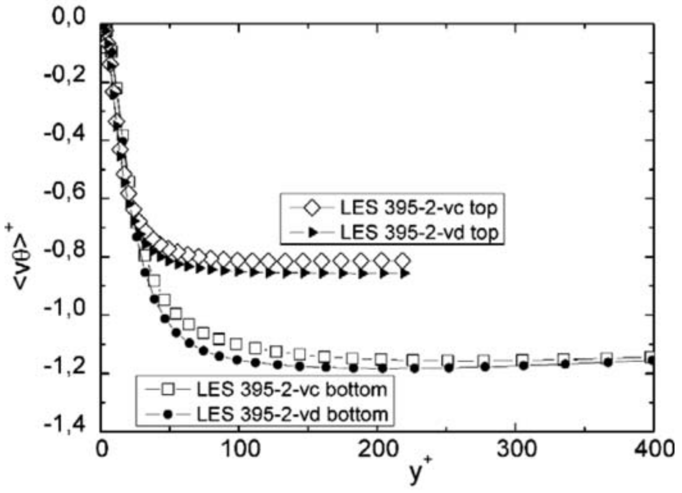

(b) Vertical velocity - temperature correlation.

Figure 12 Influence of the thermal subgrid-scale model for $T_2/T_1 = 2.00$ at $Re_{\tau m} = 395$.

ANALYSIS OF THE EFFECT OF INCREASING THE TEMPERATURE RATIO

We now focus on the impact of the temperature gradient on the turbulent flow for $Re_{\tau m} \approx 180$ and 395. Following the conclusions of the previous section, we consider here the simulations carried out with a constant subgrid-scale Prandtl number. For low temperature ratios, we use the simulation with fixed values of the conductivity and the viscosity and for the high temperature ratio we use the simulations where the variations of λ and μ are taken into account. Therefore, we compare first the cases 180-1-cc and 180-2-vc for $Re_{\tau m} \approx 180$ and, second, the cases 395-1-cc and 395-2-vc for $Re_{\tau m} \approx 395$. We begin with the presentation of the evolution of the mean, fluctuation, and correlation profiles when T_2/T_1 increases. Then we propose an underlying physical mechanism.

Mean Profiles

The mean velocity and temperature profiles normalized using the friction velocities U_τ and the friction temperatures T_τ are plotted as a function of y^+, in Figures 13c and 13d, for $Re_{\tau m} = 180$ and in Figures 14c and d for $Re_{\tau m} = 395$.

We note that for $Re_{\tau m} \approx 180$ in the linear region, the profiles of the low and high temperature ratio cases are similar. In the logarithmic area, when T_2/T_1 is higher the profile of the cold side increases and the profile of the hot side slightly decreases.

It therefore seems that the velocity profile becomes dissymmetrical for a high temperature ratio; this effect can also be seen in Figure 13a, where the velocity is normalized using the maximum velocity and plotted as a function of y/h. Some authors have previously mentioned [5, 20] this dissymmetry but only for simulation with a weak turbulent intensity ($Re_{\tau m} \leq 180$).

Always in Figure 13a, the high temperature ratio curve is a little above the low temperature ratio one near the cold wall ($y/h = 0$) and then it is slightly under the low temperature ratio one farther away from the wall. On the hot side the effect is reversed: The profile related to $T_2/T_1 = 2.00$ is under the profile related to $T_2/T_1 = 1.01$ close to the hot wall ($y/h = 2$) and above this profile closer to the channel centerline. As a consequence, the velocity gradients are modified when T_2/T_1 increases. This, in addition of the variations of the fluid properties, explains the difference between the turbulent Reynolds numbers of the bottom and top walls for $T_2/T_1 = 2.00$ (Table 2). These changes also induce a small shift of the velocity maximum, which is reached slightly closer to the hot wall.

For the mean temperature, the profiles of simulations 180-1-cc and 180-2-vc are very close (Figure 13d). However, we notice a small gap between the three curves for $y^+ \geq 80$. When looking at Figure 13b, where the temperature is normalized using the temperature difference $(T_2 - T_1)$ and the vertical coordinate is divided by the channel half height, h, we can see a deviation between the weakly and the strongly non-isothermal profiles. The curve corresponding to $T_2/T_1 = 2.00$ is slightly above the curve corresponding to $T_2/T_1 = 1.01$ all along the channel. Consequently, when the temperature ratio rises, the mean temperature profile becomes dissymmetrical, as observed by Wang and Pletcher [5] and Nicoud [20], and the average temperature has not reached at the channel centerline anymore but is closer to the cold wall (at $y/h \approx 0.92$). The temperature gradients are then not the same as the low temperature ratio case and are different on the cold and hot halves of the domain.

With a turbulent Reynolds number of 395, increasing T_2/T_1 has the same influence on the mean velocity and temperature profiles than for $Re_{\tau m} = 180$ (Figure 14).

Moreover, the deviations between the curves corresponding to the low and the high temperature ratios are stronger for this turbulent Reynolds number than for $Re_{\tau m} \approx 180$. This is particularly striking for the mean temperature profiles. Indeed, we note that the curves do not collapse since $y^+ \approx 20$ in Figure 14d,

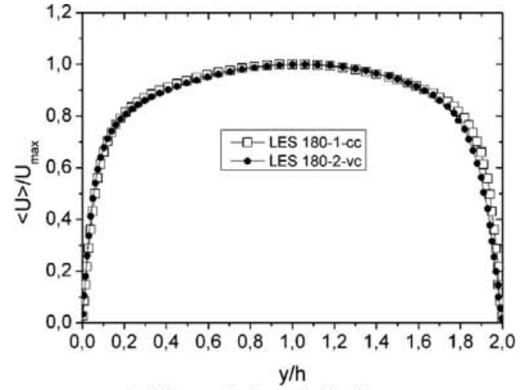

(a) Mean velocity scaled by Umax.

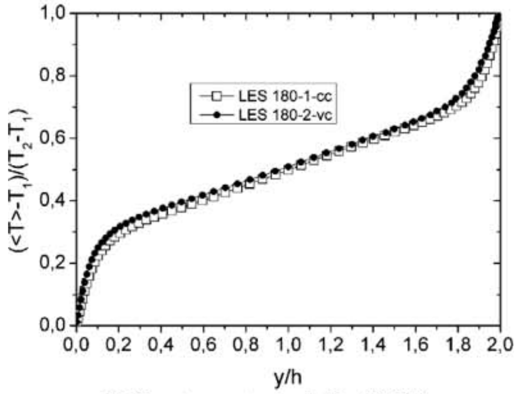

(b) Mean temperature scaled by (T2-T1).

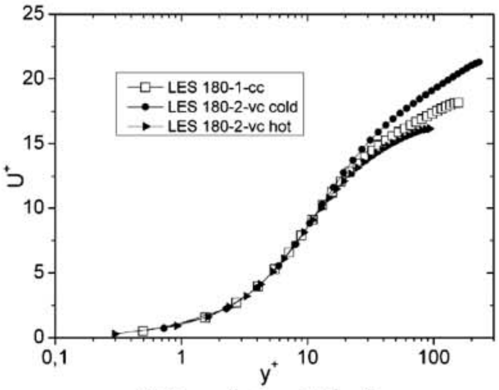

(c) Mean velocity scaled by U_τ.

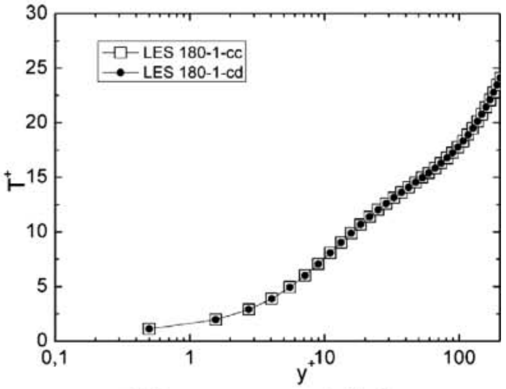

(d) Mean temperature scaled by T_τ.

Figure 13 Influence of T_2/T_1 at $Re_{\tau m} = 180$: mean velocity and temperature.

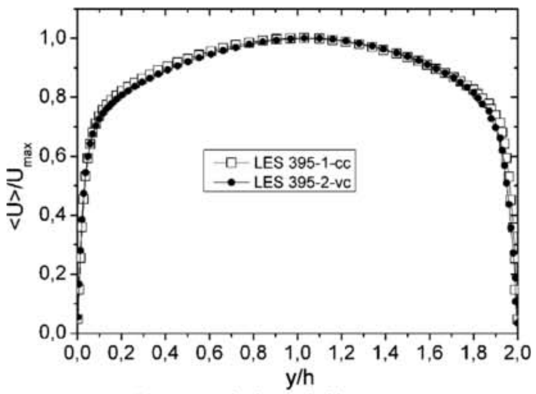

(a) Mean velocity scaled by Umax.

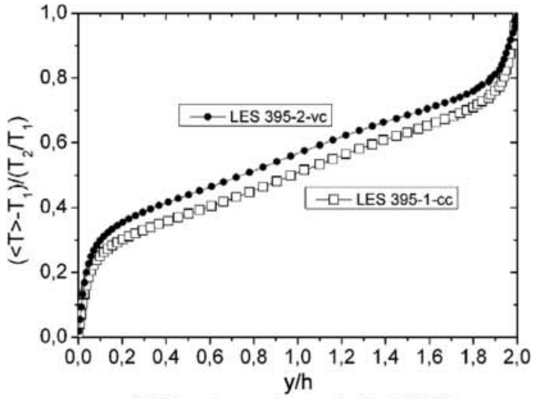

(b) Mean temperature scaled by (T2-T1).

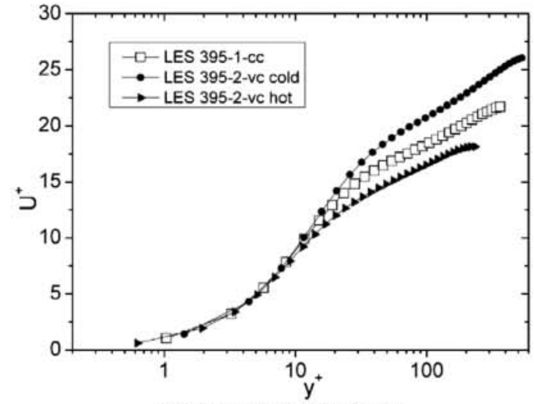

(c) Mean velocity scaled by U_τ.

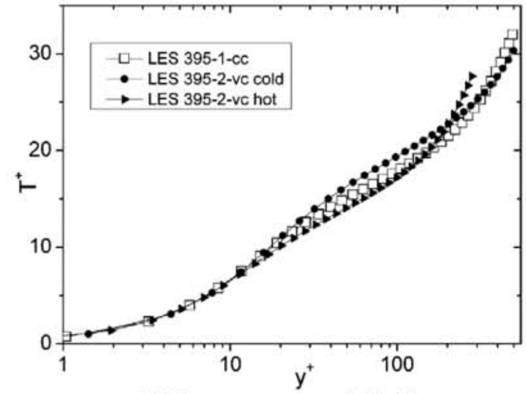

(d) Mean temperature scaled by T_τ.

Figure 14 Influence of T2/T1 at Reτm = 395: mean velocity and temperature.

and in Figure 14b the strongly non-isothermal profile is really higher than the weakly non-isothermal profile.

Fluctuations

The velocity and temperature fluctuations given by the thermal large eddy simulations 180-1-cc and 180-2-vc ($Re_{\tau m} = 180$) are compared in Figure 15 and those given by simulations 395-1-cc and 395-2-vc ($Re_{\tau m} = 395$) are shown in Figure 16.

The impact of a rise in the temperature ratio on the velocity fluctuations is the same for both turbulent Reynolds numbers. It can be seen in Figures 15a–c that T_2/T_1 strongly influences the longitudinal, vertical, and transverse velocity fluctuations. We again observe that the profiles become dissymmetrical when the temperature ratio increases. This effect is much more obvious than for the mean profiles. On the cold side of the channel, the levels of the velocity fluctuations are strongly enhanced. On the hot side, on the contrary, their levels are clearly reduced. It must also be noticed that when T_2/T_1 is higher, the locations of the peaks maxima are shifted away from the wall on the cold half of the channel and toward the wall on the hot half.

When the temperature ratio increases, the temperature fluctuations are modified too. The comparison of the curves obtained for a turbulent Reynolds number of $Re_{\tau m} = 180$ is displayed in Figure 15d. On the cold side, the profile given by the high temperature ratio simulation is above the profile of the low temperature ratio simulation in the near-wall area and for $y^+ \geq 95$ it is the contrary. On the hot side of the channel, the curves obtained in simulations 395-1-cc and 395-2-vc collapse for $0 \leq y^+ \leq 35$. For $y^+ > 35$, the level of the temperature fluctuation corresponding to the strongly non-isothermal case is higher than in the weakly non-isothermal case. In regard to the peak position, it is unchanged on the upper (hot) side but it is slightly shifted away from the wall on the lower (cold) side.

For $Re_{\tau m} \approx 395$, we can see in Figure 16d that the temperature fluctuations are more strongly modified when T_2/T_1 increases. On the cold half of the domain, the peak intensity is increased and then for $y^+ \geq 180$ the level of the temperature fluctuations diminishes. On the hot half the effect is reversed: the profile of Trms is reduced around the peak and beyond $y^+ = 80$ it is greatly enhanced. The peak location is also shifted when the temperature ratio rises: It moves slightly away from the wall on the cold side and toward the wall on the hot side.

Velocity–Velocity and Velocity–Temperature Correlations

The velocity–velocity and velocity–temperature correlations obtained for both turbulent Reynolds numbers are displayed in Figures 17 ($Re_{\tau m} \approx 180$) and 18 ($Re_{\tau m} \approx 395$). As for the velocity fluctuations, we note large gaps between the profiles of the low temperature ratio and the high temperature ratio simulations.

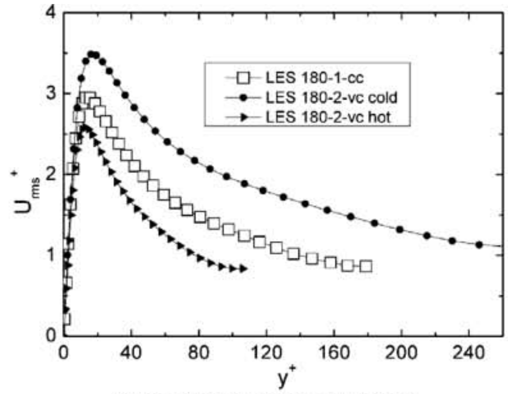

(a) Longitudinal velocity fluctuations.

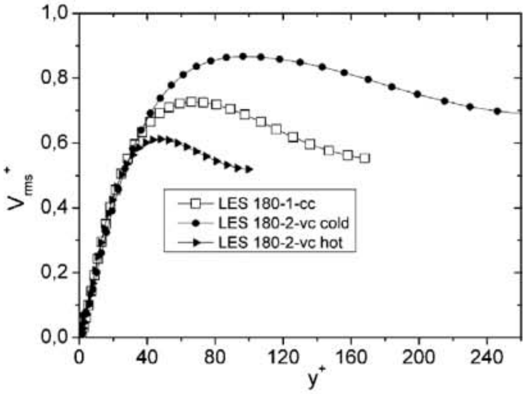

(b) Vertical velocity fluctuations.

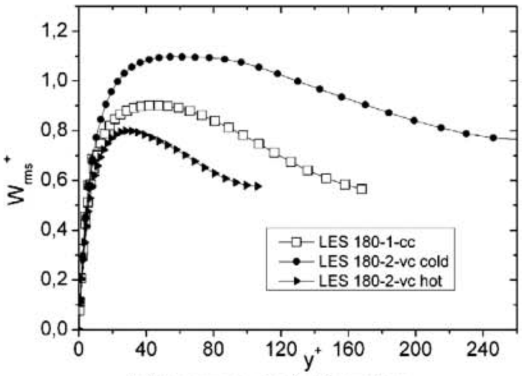

(c) Transverse velocity fluctuations.

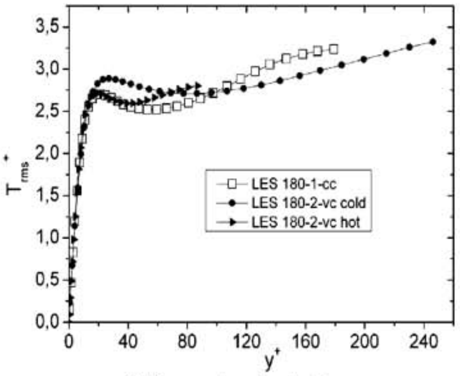

(d) Temperature fluctuations.

Figure 15 Influence of T_2/T_1 at $Re_{\tau m} = 180$: velocity and temperature fluctuations.

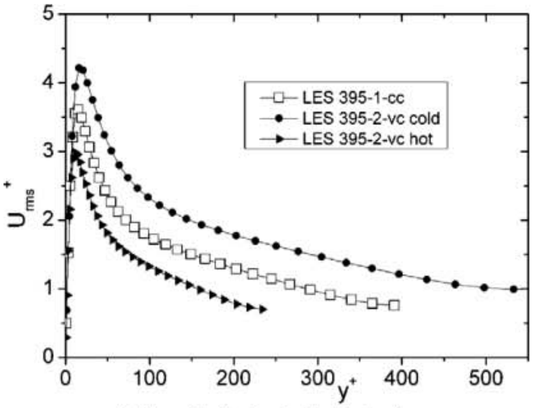

(a) Longitudinal velocity fluctuations.

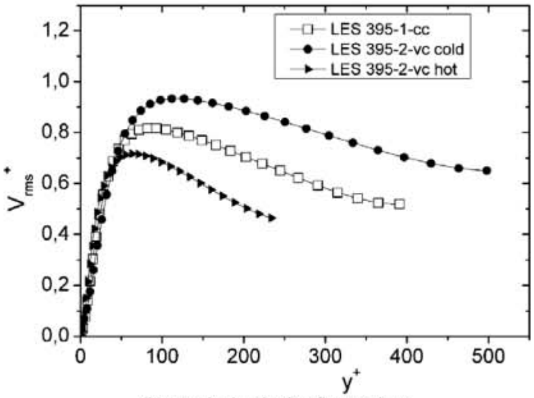

(b) Vertical velocity fluctuations.

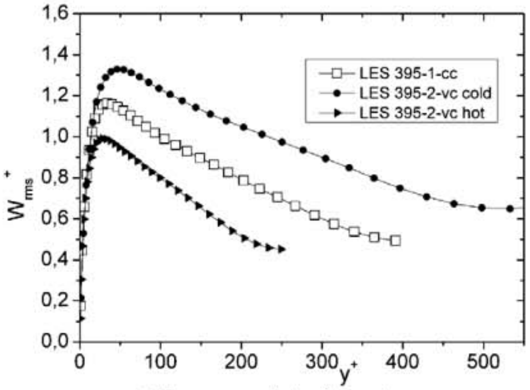

(c) Transverse velocity fluctuations.

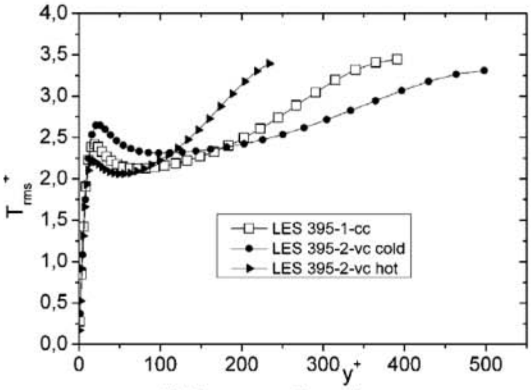

(d) Temperature fluctuations.

Figure 16 Influence of T_2/T_1 at $Re_{\tau m} = 395$: velocity and temperature fluctuations.

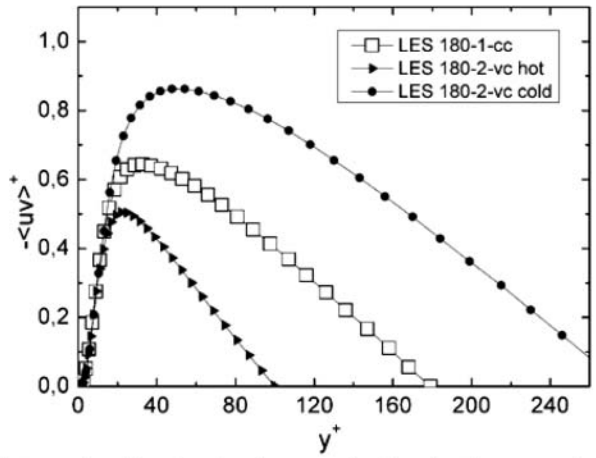

(a) Longitudinal velocity-vertical velocity correlation.

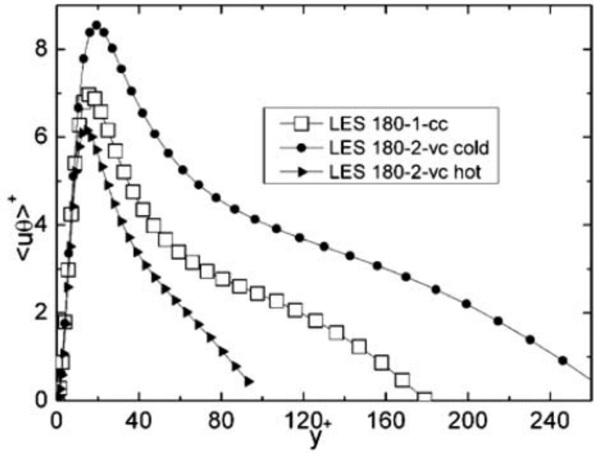

(b) Longitudinal velocity-temperature correlation.

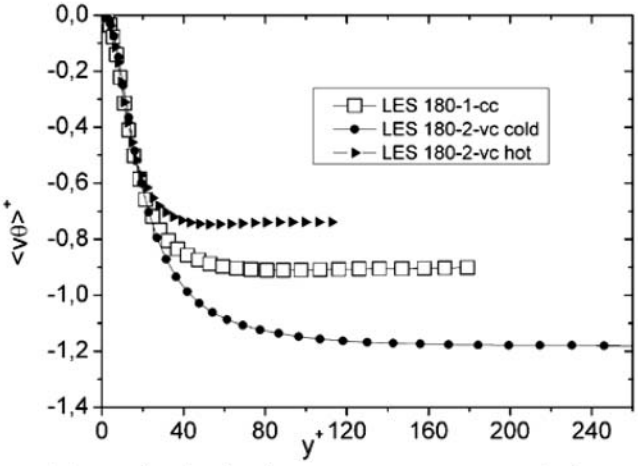

(c) Vertical velocity - temperature correlation.

Figure 17 Influence of T_2/T_1 at $Re_{\tau m} = 180$: velocity–velocity and velocity–temperature correlations.

The consequence of increasing T_2/T_1 is similar for $Re_{\tau m} \approx 180$ and $Re_{\tau m} \approx 395$. For the velocity-velocity correlation (Figure 17a) and the longitudinal velocity-temperature correlation (Figure 17b), the effect is the same than for the velocity fluctuations: On the cold side of the channel, the profiles levels become much higher and the peaks are slightly shifted away from the wall and on the hot side the profiles intensities are reduced and the peaks get a little closer to the wall. For the vertical velocity-temperature correlation profiles (Figure 17c), the evolution is similar when the temperature ratio increases if we consider their absolute values.

Effect of Semilocal and Van Driest Scalings

Up to this point, we have compared simulations using friction velocity and temperature scaling. In this section, we use semilocal and Van Driest scalings.

The semilocal scaling is performed using the following equations

$$U^*_\tau = \sqrt{\frac{\tau_w}{<\rho>(y)}} \quad ; \quad T^*_\tau = \frac{Q_w}{<\rho>(y)\,C_P U_\tau} \quad ;$$

$$y^* = \frac{yU^*_\tau}{<\nu>(y)} \tag{26}$$

We can see, in Figures 19, the longitudinal mean velocity in Figure 19a, the longitudinal velocity fluctuations in Figure 19b, and the temperature fluctuations in Figure 19c, for the simulation 395-2 using the semilocal scaling. We observe that for the longitudinal mean velocity (Figure 19a) and the longitudinal velocity fluctuations (Figure 19b), the semilocal scaling permits us to obtain closer results between the hot and the cold sides by comparison with the friction velocity scaling (Figures 14c and 16a). The dissymmetry remains for $y^I = 10$ to 300. On the other hand, for the fluctuation temperature profiles (Figure 19c) and by comparison with Figure 16d, the semilocal scaling does not reduce the dissymmetry.

The Van Driest scaling for a low Mach flow is calculated as follows [40]:

$$U^+_{VD} = \frac{-2}{\mathrm{Pr}_{sgs}\,T_\tau/T_w}\left[\sqrt{1 - \underset{sgs}{\mathrm{Pr}}\,T_\tau/T_w U^+} - 1\right] \tag{27}$$

In Figure 20 is plotted the longitudinal mean velocity using Van Driest scaling. By comparison to Figure 14c, the profiles obtained on the hot and the cold sides are closer using Van Driest scaling than using friction velocity scaling.

Taking into account the fluid property variations (semilocal or Van Driest scalings) does not permit us to suppress the dissymmetry. The coupling between turbulence and heat transfer is more complex than a simple effect of the temperature on the fluid properties.

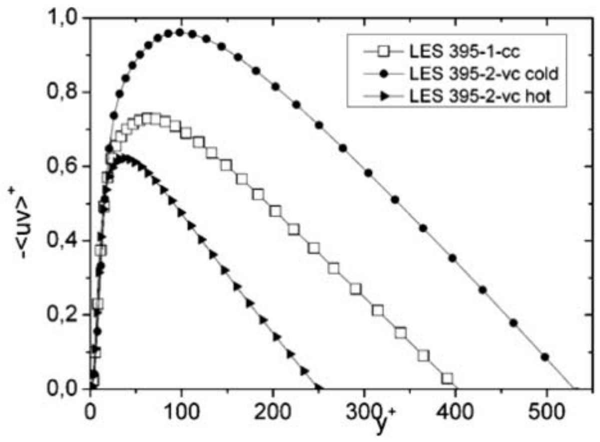

(a) Longitudinal velocity - vertical velocity correlation.

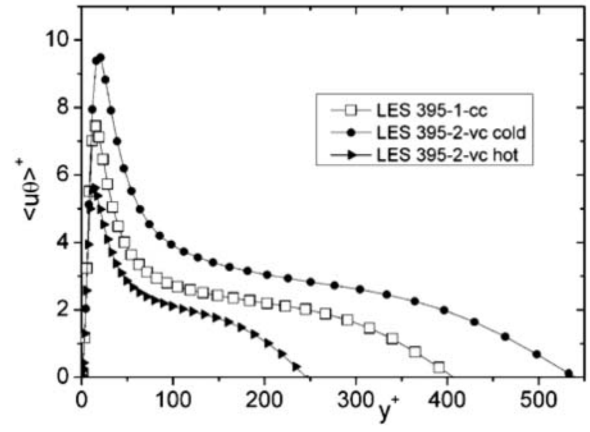

(b) Longitudinal velocity - temperature correlation.

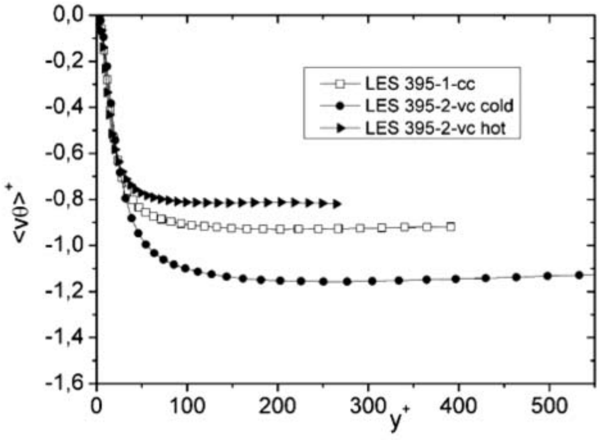

(c) Vertical velocity - temperature correlation.

Figure 18 Influence of T2/T1 at Reτm = 395: velocity–velocity and velocity–temperature correlations.

DISCUSSION OF THE PROFILE EVOLUTION

The influences of the temperature ratio on the mean profiles, on the fluctuations, and on the correlations have been described. We now turn our attention to the physical

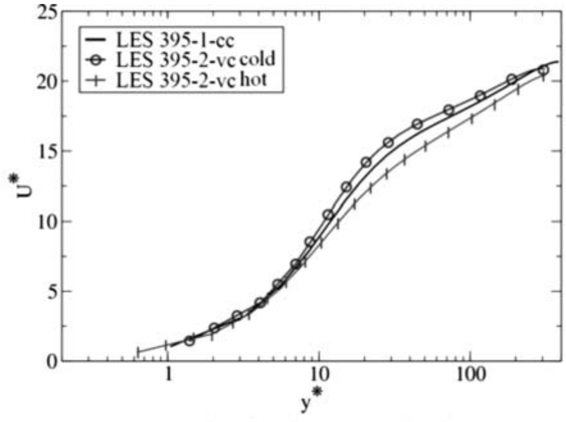

(a) Longitudinal mean velocity.

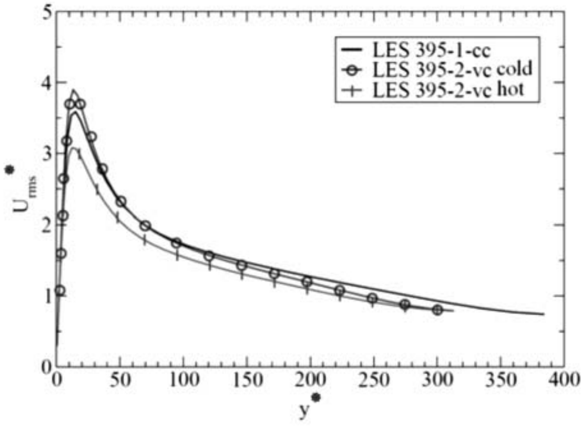

(b) Longitudinal velocity fluctuations.

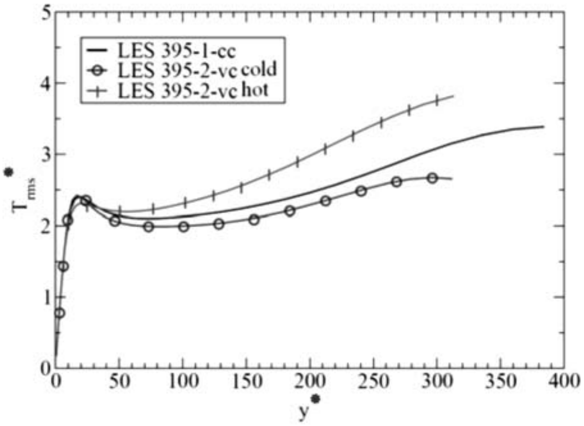

(c) Temperature fluctuations.

Figure 19 Semilocal scaling for the simulation 395-2.

mechanism that could explain the observed modifications. A diagram of this mechanism is given in Figure 21. It presents the phenomena created for the non-isothermal case ($T_2/T_1 = 2$).

We know that the temperature imposed on the top wall is twice higher than the temperature imposed on the bottom wall. This difference of temperature will directly affect all the fluid properties but in opposite manner on the two sides. Indeed, one gets:

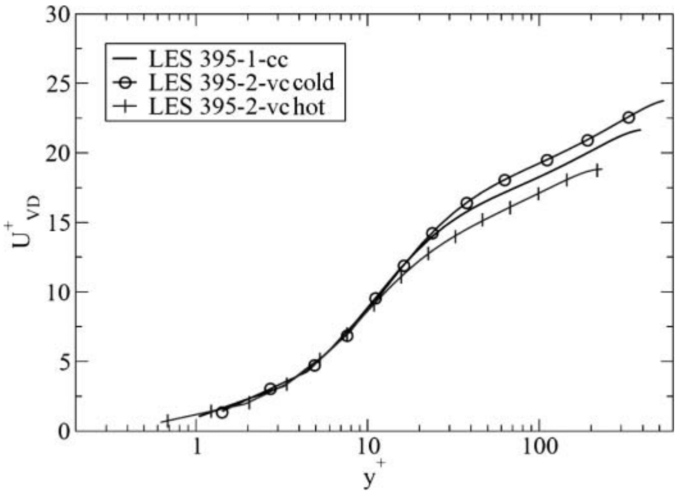

Figure 20 Van Driest scaling for the velocity, simulation 395-2.

- T_2 higher than T_1 induces ρ_2 lower than ρ_1 ($\rho = \frac{P_{thermo}}{RT}$).
- T_2 higher than T_1 induces μ_2 higher than μ_1 ($\mu(T) = 1.461\ \ 10^{-6}\frac{T^{1.5}}{T+111}$).
- T_2 higher than T_1 induces λ_2 higher than λ_1 ($\lambda(T) = \frac{\mu C_P}{\mathrm{Pr}} = \frac{1.468\ \ 10^{-3}}{\mathrm{Pr}}\frac{T^{1.5}}{T+111}$).

The large variations of ρ, μ, and λ (Table 4) when $T_2/T_1 = 2$ affect the flow through the following mechanism. The ρ and μ variations (respectively ρ and λ variations) induce significant differences for the velocity gradients (respectively temperature gradients). The differences of velocity and temperature gradients near the two walls (Table 4) result in a loss of symmetry in the velocity and temperature profiles for the whole domain. However, the relations between the fluctuations and these gradients are not linear. As a consequence, we cannot predict a priori the evolution of Urms, Vrms, Wrms, and Trms. Finally, the density profile becomes dissymmetric due to the dissymmetry of the mean temperature profile. This dissymmetry results in the redistribution of the mass flow rate, $D_m = L_z \int_{y=0}^{L_y} \rho(y)\, U(y)\, dy$, through the domain when T_2/T_1 increases. This mechanism raises the

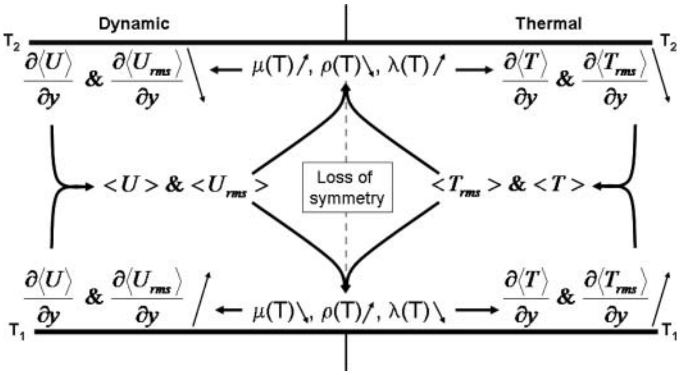

Figure 21 Physical mechanisms responsible for the modifications of all the profiles when T_2/T_1 increases ($T_2/T_1 = 1$, 1.01, 1.07 and 2).

Table 4 Values of the fluid properties and velocity and temperature gradients to the wall

Case	ρ	μ	λ	$\left.\frac{\partial<\tilde{U}>}{\partial y}\right\|_w$	$\left.\frac{\partial<\tilde{T}>}{\partial y}\right\|_w$	$\left.\frac{\partial<Urms>}{\partial y}\right\|_w$	$\left.\frac{\partial<Trms>}{\partial y}\right\|_w$
180-2-vc Cold	1.189	1.814×10^{-5}	0.0240	4.7×10^{3}	7.7×10^{4}	2.1×10^{3}	3.1×10^{4}
180-2-vc Hot	0.595	2.974×10^{-5}	0.0393	2.5×10^{3}	3.5×10^{4}	9.2×10^{2}	1.4×10^{4}
395-2-vc Cold	1.189	1.814×10^{-5}	0.0256	2.1×10^{4}	1.4×10^{5}	9.8×10^{3}	5.1×10^{4}
395-2-vc Hot	0.595	2.974×10^{-5}	0.0421	1.3×10^{4}	5.8×10^{4}	6.3×10^{3}	2.1×10^{4}

Table 5 Heat transfer coefficient (W K^{-1} m^{-2})

Side	395-1.07	395-2
Cold	18 W K^{-1} m^{-2}	25 W K^{-1} m^{-2}
Hot	17 W K^{-1} m^{-2}	16 W K^{-1} m^{-2}

question of the relative influence of the variations of the density compared to the variations of the conductivity and the viscosity. We can state that in the physical mechanism described earlier, the evolutions of the profiles are mainly due to the variations of the density, but not only to this. We showed in this article that the variations of λ and μ are not negligible. However, the impact of the variations of λ and μ is less important than the impact of ρ. Indeed, the effect of a high temperature ratio (dissymmetry of the profiles) is important even if λ and μ are assumed to be constant (Figures 5–7). Furthermore, the use of semilocal or Van Driest scaling does not contain the physic that is responsible for the dissymmetry. Consequently, the coupling between turbulence and heat transfer must be taken into account.

Another important effect of the temperature ratio concerns the heat transfer coefficient. For a turbulent Reynolds number of 395, the coefficients calculated using the results of the thermal large eddy simulations are given in Table 5. For the same turbulent Reynolds number, when the temperature ratio increases, the heat transfer coefficient increases in the cold side and decreases in the hot side. This effect is linked to the relaminarization in the hot side. It is a major inconvenience of the asymmetric heating of high-temperature solar receivers.

CONCLUSIONS

We investigated a subsonic non-isothermal turbulent channel flow representative of the flow inside a solar receiver using thermal large eddy simulation with the low Mach number equations. We studied two turbulent Reynolds numbers ($Re_{\tau m} \approx 180$ and 395) and considered low and high temperature ratios ($T_2/T_1 =$ 1.01, 1.07, and 2.00).

We first investigated the influence of the variations of the viscosity and the conductivity. We showed that for a low temperature ratio they can be fixed at constant values without changing the profiles. However, when $T_2/T_1 = 2.00$, these variations must be taken into account. We then compared two thermal subgrid-scale models: a constant subgrid-scale Prandtl number and a dynamic calculation of the subgrid-scale Prandtl number. Our results tend to demonstrate that they both give similar results, even for a temperature ratio as high as $T_2/T_1 = 2.00$. Additional simulations with a higher temperature ratio need to be carried out in order to definitely conclude as regards the thermal subgrid-scale modeling.

The modifications induced by a rise in the temperature ratio are analyzed. We observed for both $Re_{\tau m} \approx 180$ and $Re_{\tau m} \approx 395$ that when T_2/T_1 increases, the profiles become dissymmetric. Moreover, the levels and the locations of the peaks of the fluctuations and correlations are modified. Finally, we presented an explanation of the physical mechanism responsible for these changes. They are due to the combination of the variations of the fluid properties, mainly those of the density, and of their effect on the velocity and temperature gradient in the near wall region.

The results presented in this article show that the flow inside a solar receiver is driven by a complex coupling between the temperature gradient and the turbulence. This interaction is not totally included in the semilocal or Van Driest scalings. Furthermore, the heat transfer coefficient cannot be precisely determined using correlations and accurate simulations are required.

NOMENCLATURE

C_P	calorific capacity, $C_P = 1005$ J kg^{-1} K^{-1}
h	channel half height, h = 0.015, m
P_{thermo}	thermodynamic pressure, Pa
P’	corrected dynamic pressure, Pa
Pr	Prandtl number
Q_w	heat flux to the wall, W m^{-2}
Re_b	bulk Reynolds number, $Re_b = \rho_b h U_b / \mu_b$
Re_τ	wall Reynolds number, $Re_\tau = \rho w h U \tau / \mu w$
$\tilde{S}_{ij}$	strain tensor, $\tilde{S}_{ij} = \frac{1}{2}\left(\frac{\partial \tilde{U}_i}{\partial x_j} + \frac{\partial \tilde{U}_J}{\partial x_I}\right)$
T	temperature, K
T_b	bulk temperature, $T_b = \frac{1}{2h}\int_0^{2h} < \tilde{T} > (y)\, dy$
T_m	average temperature, $T_m = \frac{T_1+T_2}{2}$
T_τ	friction temperature, $T_\tau = Q_w/\rho_w C_p U_\tau$, K
T_τ^*	semilocal temperature, $T_\tau^* = \frac{Q_w}{<\rho>(y) C_P U_\tau}$
U	longitudinal velocity, m s^{-1}
U_b	bulk velocity, $U_b = \frac{1}{2h}\int_0^{2h} < \tilde{U} > (y)\, dy$
U_τ	friction velocity, $U_\tau = \sqrt{\tau_w/\rho_w}$
$U_\tau{}^*$	semilocal velocity, $U_\tau^* = \sqrt{\frac{\tau_w}{<\rho>(y)}}$

U^+_{VD}	Van Driest scaling, $U^+_{VD} = \frac{-2}{\mathrm{Pr}_{\mathrm{sgs}}\, T_\tau/T_w}\left[\sqrt{1-\mathrm{Pr}_{\mathrm{sgs}}\, T_\tau/T_w U^+}-1\right]$
V	vertical velocity, m s^{-1}
W	transverse velocity, m s^{-1}
y^+	nondimensionalized coordinate,

Greek Symbols

κ	thermal diffusivity, $\mathrm{m}^2\ \mathrm{s}^{-1}$
λ	thermal conductivity, W $\mathrm{m}^{-2}\ \mathrm{K}^{-1}$
μ	dynamic viscosity, kg $\mathrm{m}^{-1}\ \mathrm{s}^{-1}$
ν	kinematic viscosity, $\mathrm{m}^{-2}\ \mathrm{s}^{-1}$
ρ	density, kg m^{-3}
$\Im_j$	subgrid-scale heat flux, W m^{-2}
τ_{ij}	subgrid-scale stress tensor, Pa
τ_{w}	wall shear stress, $\tau_{\mathrm{w}} = \mu_{\mathrm{w}} \partial \tilde{U} / \partial y \vert w$, Pa

Subscripts

m	average value
w	value at the wall
1	value at the cold (bottom) wall
2	value at the hot (top) wall
sgs	subgrid scale

Superscripts

+	obtained using friction scaling
*	obtained using semi-local scaling

Mathematical Operators

–	operator of Reynolds meaning
∼	operator of Favre meaning

REFERENCES

[1] Huang, P. G., Coleman, G. N., and Bradshaw, P., Compressible Turbulent Channel Flows: DNS Results and Modeling, *Journal of Fluid Mechanics*, vol. 305, pp. 185–218, 1995.

[2] Coleman, G. N., Kim, J., and Moser, R. D., A Numerical Study of Turbulent Supersonic Isothermal-Wall Channel Flow, *Journal of Fluid Mechanics*, vol. 305, pp. 159–183, 1995.

[3] Morinishi, Y., Tamano, S., and Nakabayashi, K., Direct Numerical Simulation of Compressible Turbulent Channel Flow Between Adiabatic and Isothermal Walls, *Journal of Fluid Mechanics*, vol. 502, pp. 273–308, 2004.

[4] Tamano, S., and Morinishi, Y., Effect of Different Thermal Wall Boundary Conditions on Compressible Turbulent Channel Flow at m = 1.5, *Journal of Fluid Mechanics*, vol. 548, pp. 361–373, 2006.

[5] Wang, W. P., and Pletcher, R. H., On the Large Eddy Simulation of a Turbulent Channel Flow With Significant Heat Transfer, *Physics of Fluids*, vol. 8(12), pp. 3354–3366, 1996.

[6] Dailey, L. D., Meng, N., and Pletcher, R. H., Large Eddy Simulation of Constant Heat Flux Turbulent Channel Flow With Property Variations: Quasi-Developed Model and Mean Flow Results, *Journal of Heat Transfer*, vol. 125, pp. 27–38, 2003.

[7] Paolucci, S., On the Filtering of Sound From the Navier Stokes Equations, Tech. Rep. SAND82–8253, Sandia National Laboratories, Livermore, 1982.

[8] Majda, A., and Sethian, J., The Derivation and Numerical Solution of the Equations for ZeroMach Number Combustion, *Combustion Science and Technology*, vol. 42, pp. 185–205, 1985.

[9] Cook, A. W., and Riley, J. J., Direct Numerical Simulation of a Turbulent Reactive Plume on a Parallel Computer, *Journal of Computational Physics*, vol. 129(2), pp. 263–283, 1996.

[10] Debusschere, B., and Rutland, C. J., Turbulent Scalar Transport Mechanisms in Plane Channel and Couette Flows, *International Journal of Heat and Mass Transfer*, vol. 47, pp. 1771–1781, 2004.

[11] Lessani, B., and Papalexandris, M., Time-Accurate Calculation of Variable Density Flows With Strong Temperature Gradients and Combustion, *Journal of Computational Physics*, vol. 212, pp. 218–246, 2006.

[12] Lessani, B., and Papalexandris, M., Numerical Study of Turbulent Channel Flow With Strong Temperature Gradient, *International Journal of Numerical Methods for Heat and Fluid Flow*, vol. 18, pp. 545–556, 2007.

[13] Brun, C., Aubrun, T., and Ravier, P., Coherent Structures and Their Frequency Signature in the Separated Shear Layer on the Sides of a Square Cylinder, *Flow Turbulence Combustion*, vol. 81, pp. 97–114, 2008.

[14] Satake, S., Kunugi, T., Shehata, A. M., and McEligot, D. M., Direct Numerical Simulation on Laminarization of Turbulent Forced Gas Flows in Circular Tubes With Strong Heating, in *1st Symposium of Turbulence and Shear Flow Phenomena*, ed. Banerjee, Santa Barbara, CA, September 1999.

[15] Lee, J. S., Xu, W., and Pletcher, H., Large Eddy Simulation of Heated Vertical Annular Pipe Flow in Fully Developed Turbulent Mixed Convection, *International Journal of Heat and Mass Transfer*, vol. 47, pp. 437–446, 2004.

[16] Xu, X., Lee, J. S., Pletcher, R. H., Shehata, A. M., and McEligot, D. M., Large Eddy Simulation of Turbulent Forced Gas Flows in Vertical Pipes With High Heat Transfer Rates, *International Journal of Heat and Mass Transfer*, vol. 47, pp. 4113–4123, 2004.

[17] Bae, J. H., Yoo, J. Y., Choi, H., and McEligot, D. M., Effects of Large Density Variation on Strongly Heated Internal Air Flows, *Physics of Fluids*, vol. 18, pp. 075102-1–075102-25, 2006.

[18] Qin, Z., and Pletcher, R. H., Large Eddy Simulation of Turbulent Heat Transfer in a Rotating Square Duct, *International Journal of Heat and Fluid Flow*, vol. 27, pp. 371–390, 2006.

[19] Nicoud, F., Conservative High-Order Finite-Difference Schemes for Low-Mach Number Flows, *Journal of Computational Physics*, vol. 158, pp. 71–97, 2000.

[20] Nicoud, F., Numerical Study of a Channel Flow With Variable Properties, *CTR Annual Research Briefs*, pp. 289–309, 1998.

[21] Lesieur, M., Métais, O., and Comte, P., *Large-Eddy Simulations of Turbulence*, Cambridge University Press, Cambridge, p. 219, 2005.

[22] Serra, S., Husson, S., and Bataille, F., Interaction Between a Turbulent Flow and Heat Transfers in High Temperature Solar Receivers, SolarPaces, Las Vegas, NV, p. 8, 2008.

[23] Speziale, C. G., Erlebacher, G., and Hussaini, M. Y., The Subgrid-Scale Modelling of Compressible Turbulence, *Physics of Fluids*, vol. 31, pp. 940–943, 1988.

[24] Elmo, M., and Cioni, O., Low Mach Number Model for Compressible Flows and Application to HTR, *Nuclear Engineering and Design*, vol. 222, pp. 117–124, 2003.

[25] Nicoud, F., and Ducros, F., Subgrid-Scale Stress Modeling Based on the Square of the Velocity Gradient Tensor, *Flow, Turbulence and Combustion*, vol. 62, pp. 183–200, 1999.

[26] Nicoud, F., and Poinsot, T., DNS of a Channel Flow With Variable Properties, 1st International Symposium on Turbulence and Shear Flow Phenomena, 1999.

[27] Moin, P., Squires, K., Cabot, W., and Lee, S., A Dynamic Subgrid-Scale Model for Compressible Turbulence and Scalar Transport, *Physics of Fluids*, vol. 3(11), pp. 2746–2757, 1991.

[28] Moin, P., and Kim, J., Numerical Investigation of Turbulent Channel Flow, *Journal of Fluid Mechanics*, vol. 118, pp. 341–377, 1982.

[29] Jimenez, J., and Moin, P., The Minimal Flow Unit in Near-Wall Turbulence, *Journal of Fluid Mechanics*, vol. 225, pp. 213–240, 1991.

[30] Brillant, G., Husson, S., and Bataille, F., Large Eddy Simulations of Heat and Mass Transfer in Case of Non Isothermal Blowing, *Engineering Turbulence Modeling and Experiments*, vol. 6, pp. 751–760, ERCOFTAC, Sardinia, Italy, 2005.

[31] Châtelain, A., Ducros, F., and Métais, O., LES of Turbulent Heat Transfer: Proper Convection Numerical Schemes for Temperature Transport, *International Journal for Numerical Methods in Fluids*, vol. 44(9), pp. 1017–1044, 2004.

[32] Pham, F., Plourde, M.V., and Doan K. S., Direct and Large-Eddy Simulations of a Pure Thermal Plume, *Physics of Fluids*, vol. 19, p. 13, 2007.

[33] Seok Choi, K., and Suzuki, H., Large Eddy Simulation of Turbulent Flow and Heat Transfer in Channel With One Wavy Wall, *International Journal of Heat and Fluid Flow*, vol. 26, pp. 681–694, 2005.

[34] Sagaut, P., Compte, P., and Ducros, F., Filtered Subgrid-Scale Models, *Physics of Fluids*, vol. 12(1), pp. 233–236, 2007.

[35] Lee, J. S., and Pletcher, H., Large Eddy Simulation of Variable Property Turbulent Flow in Horizontal and Vertical Channels With Buoyancy and Heat Transfer Effects, *Proc. Institution of Mechanical Engineers, Part C, Mechanical Engineering Science*, vol. 221(4), pp. 429–441, 2007.

[36] Kim, J., Moin, P., and Moser, R., Turbulence Statistics in Fully Developed Channel Flow at Low Reynolds Number, *Journal of Fluid Mechanics*, vol. 177, pp. 133–166, 1987.

[37] Moser, R. D., Kim, J., and Mansour, N. N., Direct Numerical Simulation of Turbulent Channel Flow up to re$\tau = 590$, *Physics of Fluids*, vol. 11(4), pp. 943–945, 1999.

[38] Kawamura, H., Abe, H., and Matsuo, Y., DNS of Turbulent Heat Transfer in Channel Flow With Respect to Reynolds and Prandtl Number Effect, *Journal of Heat and Fluid Flow*, vol. 20, pp. 196–207, 1999.

[39] Brillant, G., Husson, S., and Bataille, F., Subgrid-Scale Diffusivity: Wall Behavior and Dynamic Methods, *ASME Journal of Applied Mechanics*, vol. 73(3), pp. 360–367, 2006.

[40] Nicoud, F., and Bradshaw, P., A Velocity Transformation for Heat and Mass Transfer, *Physics of Fluids*, vol. 12, pp. 237–238, 2000.

Sylvain Serra is a Ph.D. student in engineering science in the Processes, Materials and Solar Energy laboratory (PROMES, UPR CNRS 8521) at the University of Perpignan Via Domitia (UPVD), France. He holds an M.Sc. in solar energy from the UPVD. His main research interest concerns the coupling between turbulence and thermal gradient in industrial processes that produce electricity.

Adrien Toutant is an assistant professor of fluid dynamics and thermal transfer in the PROMES laboratory at the UPVD, France. He holds an M.Sc. in applied mathematics from the French engineering school ENSTA and the University of Paris 6, as well as a Ph.D. degree in fluid dynamics from INP-Toulouse, France. His main research interest concerns the coupling between turbulence, multiphase flow, and thermal gradient in industrial processes that produce electricity.

Françoise Bataille works in the French Processes, Materials and Solar Energy laboratory (PROMES, UPR CNRS 8521). She holds a B.S. degree in physics from the ENS in Lyon, as well as M.Sc. and Ph.D. degrees in fluid mechanics from the Ecole Centrale in Lyon. She spent a long period at the ICASE (NASA Langley, VA) before joining the CETHIL Laboratory in Lyon, first as an associate and later as a professor. She moved to Perpignan and the PROMES laboratory in 2005. Her main research interests are in fluid mechanics and heat transfer.